Splay-induced order in systems of hard tapers

Piotr Kubala ⓘ, Michał Cieśla, and Lech Longa ⓘ

Institute of Theoretical Physics, Jagiellonian University in Kraków, Łojasiewicza 11, 30-348 Kraków, Poland

The main objective of this work is to clarify the role that taper-shaped elongated molecules, i.e., molecules with one end wider than the other, can play in stabilizing orientational order. The focus is exclusively on entropy-driven self-organization induced by purely excluded volume interactions. Drawing an analogy to RM734 (4-[(4-nitrophenoxy)carbonyl]phenyl-2,4-dimethoxybenzoate), which is known to stabilize ferroelectric nematic (N_F) and nematic splay (N_S) phases, and assuming that molecular biaxiality is of secondary importance, we consider monodisperse systems composed of hard molecules. Each molecule is modeled using six collinear tangent spheres with linearly decreasing diameters. Through hard-particle, constant-pressure Monte Carlo simulations, we study the emergent phases as functions of the ratio between the smallest and largest diameters of the spheres (denoted as d) and the packing fraction (η). To analyze global and local molecular orderings, we examine molecular configurations in terms of nematic, smectic, and hexatic order parameters. Additionally, we investigate the radial pair distribution function, polarization correlation function, and the histogram of angles between molecular axes. The last characteristic is utilized to quantify local splay. The findings reveal that splay-induced deformations drive unusual long-range orientational order at relatively high packing fractions ($\eta > 0.5$), corresponding to crystalline phases. When $\eta < 0.5$, only short-range order is affected, and in addition to the isotropic liquid, only the standard nematic and smectic-A liquid crystalline phases are stabilized. However, for $\eta > 0.5$, apart from the ordinary nonpolar hexagonal crystal, three additional frustrated crystalline polar blue phases with long-range splay modulation are observed: antiferroelectric splay crystal ($Cr_S P_A$), antiferroelectric double-splay crystal ($Cr_{DS} P_A$), and ferroelectric double-splay crystal ($Cr_{DS} P_F$). Finally, we employ Onsager-Parsons-Lee local density functional theory to investigate whether any sterically induced (anti)ferroelectric nematic or smectic-A type of ordering is possible for our system, at least in a metastable regime.

I. INTRODUCTION

The most spectacular discovery of the last decade in the field of liquid crystal research has been the identification of the ferroelectric nematic (N_F) [1–4], antiferroelectric nematic splay (N_S) [5], and nematic twist-bend (N_{TB}) [6–8] phases, all characterized by various forms of long-range polar order.

Based on current experimental observations, it seems that the stabilization of these new nematic phases is linked to the strong softening (i.e., reduction by one to two orders of magnitude) of one of the Frank elastic constants, K_{ii} [9], in the parent, uniaxial nematic (N) phase, near the transition to one of the polar nematics. Here K_{ii}s ($i = 1, 2, 3$) weight elementary deformations of splay (K_{11}), twist (K_{22}), and bend (K_{33}) types of the undistorted, reference uniaxial nematic state (N) in the Oseen-Zocher-Frank free energy [9–11]

$$\mathcal{F} = \frac{1}{2V} \int_V [K_{11}[\hat{\mathbf{n}}(\nabla \cdot \hat{\mathbf{n}})]^2 + K_{22}[\hat{\mathbf{n}} \cdot (\nabla \times \hat{\mathbf{n}})]^2$$
$$+ K_{33}[\hat{\mathbf{n}} \times (\nabla \times \hat{\mathbf{n}})]^2], \tag{1}$$

where $\hat{\mathbf{n}}$ denotes the locally preferred orientation of molecules referred to as the director, and V is the system's volume.

While each Frank elastic constant is typically positive and on the order of 10 pN, the observed softening of K_{ii} suggests that the lack of orientational modulation of N is no longer energetically favored, and it can promote the appearance of

orientationally modulated phase. Effectively, it means that the softened elastic constant may become negative. An important observation made by Meyer many years ago [12] was that this softening can be attributed to the entropy of packing of molecules with specific shape of nonzero steric dipole. In fact, the dipolar asymmetry of these molecules is expected to induce a flexopolarization effect, which couples to splay and bend director deformations [13] and effectively reduces the K_{11} and/or K_{33} elastic constants [14]. For instance, molecules with a bow (banana) shape can reduce the K_{33} bend elastic constant, leading to the formation of twist-bent and splay-bent phases [15]. Greco and Ferrarini were the first to explicitly demonstrate this phenomenon through molecular dynamics simulation on a system of bow-shaped molecules that interact solely through steric interactions [16].

Further studies on bow-shaped molecules, focusing on steric interactions, have not only provided successful explanations for the formation of the N_{TB} phase [17,18] but have also demonstrated the potential for stabilizing various intermediate polar states between N_{TB} and N_{SB} [17].

It is well known that even slight differences in the geometry of molecules can have a significant impact on the resulting liquid-crystalline self-assembly. For example, a smectic-A phase is observed in a system consisting of spherocylinders [19], whereas ellipsoids with a very similar shape do not exhibit this behavior [20]. This principle also applies to the recently discovered N_F and N_S phases. These phases rely

on both taperlike molecular anisotropy and a strong, nearly longitudinal total molecular dipole moment as crucial molecular characteristics contributing to their stability. Specifically, the taperlike molecular shapes can result in a negative K_{11} splay constant [21], thereby contributing to the formation of the polar splay nematic [14,22,23] and related smectic phases [24,25].

Numerical simulations of systems composed of wedge-like (e.g., pear-shaped, tapered, etc.) molecules began in the late 1990s [26,27]. In these simulations, shape polarity at the molecular level was induced by a soft interaction potential between molecules, which combined two rigidly connected centers: an ellipsoidal Gay-Berne potential [28] and a spherical Lennard-Jones potential. The reported liquid crystalline phases in these simulations were only ordinary uniaxial nematic and smectic phases, without any macroscopic polarization, as they exhibited a preference for antiparallel local arrangement.

Berardi, Ricci, and Zannoni developed a generalized single-site Gay-Berne potential to model the attractive and repulsive interactions between elongated tapered molecules [29]. Through parameter adjustments and Monte Carlo simulations, they observed stable N_F and ferroelectric smectic liquid crystals. However, while the introduction of a weak axial dipole did not qualitatively impact these observations, an increase in dipole strength resulted in the destruction of long-range ferroelectric ordering. It is worth noting that using a standard Gay-Berne potential with an axial dipole at one end of the molecule resulted in the formation of a bilayer smectic phase [30–32]. Similar mesophase formation was observed in simulations of single-site hard pears [33].

Purely entropic systems constructed of pear-shaped molecules also exhibit a cubic gyroid phase [34,35]. Interestingly, the stability of this phase is highly sensitive to the details of the hard-core interaction. Specifically, the cubic gyroid phase is observed when describing the pear shape using two Bézier curves with the pear hard Gaussian overlap (PHGO) model. However, it vanishes when the hard pears of revolution (HPR) model is used. In the PHGO model, a bilayer smectic phase is also observed, whereas the HPR model exhibits isotropic and nematic phases [36].

Finally, we should mention sno-cone-shaped particles studied using Monte Carlo simulations by Chen, Zhang, and Glotzer [37]. At low packing fractions (0.1–0.3), they observed the self-assembly of molecules into nanoclusters of shape solely determined by the cone angle. The conical excluded volume forced the particles to assemble into curved, closed polyhedral convex shapes.

In this paper, we seek to explore the fundamental mechanisms that can lead to the emergence of long-range splay and potentially polar order in liquid crystal systems. Specifically, we focus on the interactions among hard taper-shaped molecules in the absence of dipolar electrostatic or dispersion forces. By investigating whether such long-range order can be stabilized solely through entropic interactions, we aim to advance our understanding of the essential features of molecular interactions responsible for stabilizing N_F and N_S phases.

To achieve this goal, we utilize a model consisting of six collinear tangent spheres, resulting in a molecule with $C_{\infty v}$ (cone) symmetry [Fig. 1(a)]. The diameters of the spheres fol-
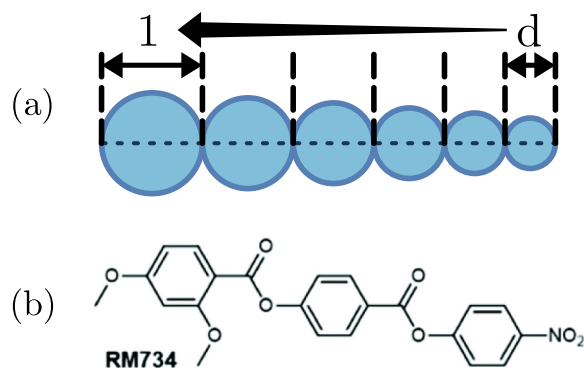

FIG. 1. (a) Family of tapers used in the study; they are built of six collinear tangent spheres with diameters increasing linearly from d to 1 ($d \leqslant 1$ is a parameter). (b) Taper-shaped RM734 molecule known to form a polar nematic phase. Reprinted from Ref. [4] with the permission of the Royal Society of Chemistry.

low an arithmetic sequence, starting from d and progressing to 1. Specifically, the diameters are given by d, $(4d + 1)/5$, $(3d + 2)/5$, $(2d + 3)/5$, $(d + 4)/5$, and 1. Here, the parameter d represents the diameter of the smallest sphere and serves as a descriptor for the shape of the molecule. When $d = 1$, the molecule reduces to the linear tangent hard-sphere (LTHS) model as described by Vega *et al.* [38]. The molecule's length is equal to $3(d + 1)$, while the mean ball diameter is $(d + 1)/2$. Thus, the molecular aspect ratio is 6 regardless of d. Alternatively, if we use the maximal ball diameter instead of its mean value, the aspect ratio is $3(d + 1)$ and consequently lies in the range [3, 6] for $d \in [0, 1]$.

We have chosen this model to capture essential features of the effective shape exhibited by the RM734 molecule (4-[(4-nitrophenoxy)carbonyl]phenyl-2,4-dimethoxybenzoate) [Fig. 1(b)]. As previously mentioned, the RM734 mesogen has been shown to stabilize N_F and N_S phases [3,4]. By utilizing a model with similar shape characteristics, we aim to gain further insight into the relationship between the entropy of packing and the resulting self-organization in liquid crystal systems. To this end, we investigate the phase diagram and properties of stable structures using Monte Carlo integration. Additionally, we compare our results with those obtained from previous studies on soft- and hard-core pear models. Furthermore, we examine how the gradient of a molecule's diameter influences the presence and extent of the observed phases.

Finally, we recognize that the anisotropic polar shape of the molecules may give rise to nontrivial dense configurations. We are particularly interested in exploring whether these configurations exhibit crystal-like or glasslike structures, considering the potential competition between different types of lattices [39–41].

The remainder of this paper is organized as follows: In Sec. II A we provide a brief description of the Monte Carlo integrator used. In Secs. II B and II C, we introduce the order parameters and correlation functions used to monitor properties of equilibrium structures. The results obtained from Monte Carlo simulations are presented in Sec. III. In Sec. IV, we formulate the Parsons-Lee density functional theory to

study polar ordering in the liquid-crystalline regime. We analyze some equilibrium and metastable phases in detail. Last, we provide a discussion and outlook in Sec. V. The Appendix contains remarks about nontilted hexagonal configurations of close-packed linear tangent hexamers.

II. METHODS

A. Monte Carlo simulations

We assumed hard-core interactions between molecules. The equilibrium phases were classified as a function of the shape parameter d and the packing fraction η. The latter one is defined as a ratio of the total volume of all molecules to the volume of a simulation box, and is a natural choice for purely steric repulsion. System snapshots were obtained numerically using the Monte Carlo (MC) scheme [42] implemented in our RAMPACK software package. Integration was carried out in the N-p-T ensemble. For hard-core interactions, only a ratio p/T of pressure and temperature is an independent parameter and can be used to control the packing fraction η. To allow relaxation of the full viscous stress tensor (including the sheer part), we used a triclinic simulation box with periodic boundary conditions. For a system of N molecules, a full MC cycle consisted of N rototranslation moves, $N/10$ flip moves, and a single box move. In a rototranslation move, a single shape was chosen at random, translated by a random vector, and rotated around the random axis by a random angle (clockwise and anticlockwise rotations were equally probable to preserve the detailed balance condition). If the move introduced an overlap, it was always rejected and accepted otherwise. Flip moves were performed in a similar way to rototranslation moves; however, instead of random translation and rotation, the molecule was rotated by $180°$ around its geometric center. This type of move facilitated easier sampling of the phase space of the system, especially for high η. For a box move, the three vectors $\mathbf{b}_1$, $\mathbf{b}_2$, $\mathbf{b}_3$ that span the box were perturbed by small random vectors. The move was rejected if any overlaps were introduced. Otherwise, it was accepted according to the Metropolis-Wood criterion with probability [43,44]

$$\min\left\{1, \exp\left(N \log \frac{V}{V_0} - \frac{p\Delta V}{T}\right)\right\}, \quad (2)$$

where $\Delta V = (V - V_0)$ and V_0 and V are, respectively, the volume of the box before and after the move. The perturbation ranges were adjusted during the thermalization phase to achieve an acceptance probability of around 0.15. To accelerate simulations in a modern multithreaded environment, we used the domain decomposition technique [45] for molecule moves and we parallelized independent overlap checks for volume moves.

To scan the full phase sequence, from isotropic liquid to crystal, we used p/T ratios corresponding to packing fraction covering $\eta \in [0.3, 0.58]$ for $d \in [0.4, 1.0]$. First, to roughly determine the phase boundaries, preliminary simulations were performed by gradually compressing a small system of $N = 400$ molecules in a cubic box from a highly diluted simple cubic lattice. For each p/T, the integration consisted of the thermalization run with 9.5×10^6 full MC cycles and the production run with 0.5×10^6 cycles to gather averages. The final

snapshot of a run was used as a starting point for the next with a slightly higher p/T. Using the results as guidance, the main simulations were performed on a much larger system with $N > 5000$ in a triclinic box. The initial configuration in the whole range of d was smectic A with $\eta \approx 0.45$ (see Sec. III for the description of phases) prepared by thermalizing different types of slightly diluted crystals for $(1–5) \times 10^8$ cycles. Initial configurations were then independently compressed or expanded to all target densities in parallel. Thermalization runs were performed for $(0.9–4.5) \times 10^8$ cycles, while production runs were performed for $(0.1–0.5) \times 10^8$ cycles. Additionally, in order to estimate maximal packing fractions, the densest configurations for each d were compressed under exponentially increasing pressure for 3×10^8 cycles, reaching $p/T = 10^4$ at the end.

B. Order parameters

Phases in the system can be easily classified using a carefully chosen set of order parameters, whose values have jumps on the boundaries of phase transitions. The nematic order along the director $\hat{\mathbf{n}}$ is detected by the average value $\langle P_2(\hat{\mathbf{a}} \cdot \hat{\mathbf{n}}) \rangle$ of the second-order Legendre polynomial, where $\hat{\mathbf{a}}$ is the long axis of the molecule. Director $\hat{\mathbf{n}}$ can be inferred directly from the system using the second-rank $\mathbf{Q}$ tensor [46], which can be numerically computed as

$$\mathbf{Q} = \frac{1}{N} \sum_{i=1}^{N} \frac{3}{2}\left(\hat{\mathbf{a}}_i \otimes \hat{\mathbf{a}}_i - \frac{1}{3}\right), \quad (3)$$

where the summation is done over all molecules in a single snapshot. P_2 is then the eigenvalue of $\mathbf{Q}$ with the highest magnitude, and $\hat{\mathbf{n}}$ the corresponding eigenvector. Ensemble-averaged $\langle P_2 \rangle$ is calculated by averaging P_2 over noncorrelated system snapshots. The nematic order parameter has a minimal value -0.5, when all molecules are perpendicular to $\hat{\mathbf{n}}$, and reaches its maximum 1 for molecules perfectly aligned with $\hat{\mathbf{n}}$ (please note that $\hat{\mathbf{n}}$ and $-\hat{\mathbf{n}}$ directions are equivalent). In a disordered system $\langle P_2 \rangle = 0$.

Density modulation can be quantitatively described by the smectic order parameter $\langle \tau \rangle$ [47]. It is defined as

$$\langle \tau \rangle = \frac{1}{N}\left\langle \left\| \sum_{i=1}^{N} \exp(i\mathbf{k} \cdot \mathbf{r}_i) \right\| \right\rangle, \quad (4)$$

where $\mathbf{k}$ is the modulation wave vector compatible with periodic boundary conditions (PBCs) and $\mathbf{r}_i$ is the center of the ith molecule. More precisely, by *molecule's center* we refer to the middle point of a molecule's length. As the drift of the whole system is a Goldstone mode, the absolute value $|\cdots|$ is taken before the ensemble averaging to eliminate it. All possible $\mathbf{k}$ can be enumerated using reciprocal box vectors $\mathbf{g}_1$, $\mathbf{g}_2$, $\mathbf{g}_3$ [48] and taking linear combinations of them with integer coefficients h, k, l (Miller indices [49]): $\mathbf{k} = h\mathbf{g}_1 + k\mathbf{g}_2 + l\mathbf{g}_3$. Here, as the initial configuration is always a smectic with six layers stacked along the z axis, $hkl = 006$. The smectic order ranges from 0 for a homogeneous system to 1 for a perfectly layered one.

Another feature of the system that is measured in the study is the hexatic order appearing for high packing fractions η, where molecules tend to form hcp-like structures. The local

hexatic order can be measured using the so-called hexatic bond order parameter $\langle \psi_6 \rangle$ [50]. For a two-dimensional system, it is defined as

$$\langle \psi_6 \rangle = \frac{1}{N} \left\langle \sum_{i=1}^{N} \frac{1}{6} \left| \sum_{j=1}^{6} \exp(6i\phi_{ij}) \right| \right\rangle, \qquad (5)$$

where ϕ_{ij} is the angle between an arbitrary axis in the plane and the vector that joins the center of the ith molecule with its jth-nearest neighbor. It can be generalized to three-dimensional systems by projecting the positions of molecules onto the nearest smectic layers and computing ψ_6 within the planes defined by them. Random points give $\langle \psi_6 \rangle \approx 0.37$, while a perfect hexatic order yields $\langle \psi_6 \rangle = 1$. The local hexatic order can also be computed for a system without layers by projecting all centers on a single plane.

C. Correlation functions

Additional insight into both global properties and supramolecular structures is given by correlation functions. For all correlation functions, the distance is measured between molecules' centers, i.e., midpoints of molecules' lengths. The first is a standard radial distribution function [51], which can be defined in a computationally friendly way as

$$\rho(r) = \left\langle \left\langle \frac{dN(r, r + dr)}{4\pi r^2 dr \cdot (N/V)} \right\rangle_N \right\rangle, \qquad (6)$$

where $dN(r, r + dr)$ is the number of molecules whose distance from a selected single molecule lies in the range $(r, r + dr)$, dr is the numerical size of the bin, N is the total number of molecules, and V is the volume of the system. It is then averaged over all molecules, $\langle \cdots \rangle_N$, and over independent snapshots, $\langle \cdots \rangle$. It is normalized in such a way that, for a disordered isotropic system, it approaches 1 for $r \to \infty$. In systems with long-range translational order, $\rho(r)$ has a series of numerous minima and maxima.

In a layered system, one can also measure the layerwise radial distribution function in the direction orthogonal to $\mathbf{k}$,

$$\rho_\perp(r_\perp) = \frac{1}{n_L} \left\langle \sum_{i=1}^{n_L} \left\langle \frac{dN_i(r_\perp, r_\perp + dr_\perp)}{2\pi r_\perp dr_\perp \cdot (N/S)} \right\rangle_{N_i} \right\rangle, \qquad (7)$$

where n_L is the number of layers, $dN_i(r_\perp, r + dr_\perp)$ is the number of molecules in the ith layer whose distance from a selected single molecule calculated along the layer's plane lies in the range $(r_\perp, r_\perp + dr_\perp)$, and S is the total surface area of all layers [52]. In the end, it is averaged over all molecules in the layer, $\langle \cdots \rangle_{N_i}$, all layers, $(1/n_L) \sum_{i=1}^{n_L} \cdots$, and uncorrelated system snapshots, $\langle \cdots \rangle$.

As the results will show, the system develops a nontrivial polar metastructure. To quantify it, we use the layerwise radial polarization correlation [51], defined like $\rho_\perp(r_\perp)$:

$$S_\perp^{110}(r_\perp) = \frac{1}{n_L} \left\langle \sum_{i=1}^{n_L} \langle \hat{\mathbf{a}}_{i_j} \cdot \hat{\mathbf{a}}_{i_k} \rangle_{i_j i_k} \right\rangle, \qquad (8)$$

where $\langle \cdots \rangle_{i_j i_k}$ denotes the average over all molecules in the ith layer, whose centers' distance along this layer lies in the $(r_\perp, r + dr_\perp)$ range.
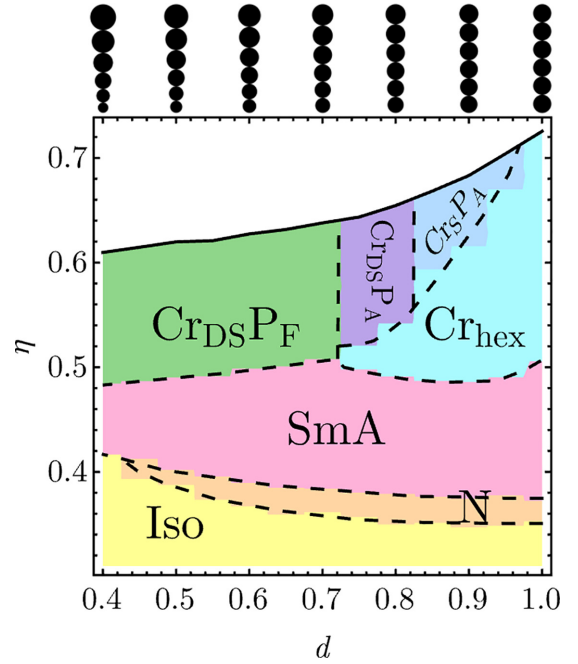

FIG. 2. Phase diagram of the system in (d, η) space. The liquid phases, isotropic (Iso), nematic (N), and smectic A (SmA), as well as crystalline ones, hexagonal crystal (Cr_{hex}), antiferroelectric double-splay crystal ($Cr_{DS}P_A$), antiferroelectric splay crystal ($Cr_S P_A$), and ferroelectric double-splay crystal ($Cr_{DS}P_F$), were recognized. The black solid line at the top boundary of the phase diagram represents the maximal packing fraction η for a given d value. The illustrative shapes above the diagram were normalized to have the same mean ball diameter.

The range of splay correlations can be quantified by the conditional probability $P(\theta|r_\perp)$ of finding two molecules with angle θ between their molecular axes $\hat{\mathbf{a}}_i$ at a transversal distance $r_\perp$, normalized as

$$\int_{0°}^{90°} P(\theta|r_\perp) d\theta = 1, \quad \forall r_\perp. \qquad (9)$$

To be consistent with the polarization correlation function, this quantity will also be calculated layerwise. As splay corresponds to the radial spread of director field lines, the most probable angle θ should grow with $r_\perp$ in systems with nonzero splay deformation mode.

III. RESULTS

Using the method described in Sec. II A, we were able to recognize all phases for $d \in [0.4, 1.0]$ and $\eta \in [0.3, 0.58]$. There are three liquid phases, isotropic liquid (Iso), nematic (N), and smectic A (SmA), and four crystalline phases, hexagonal crystal (Cr_{hex}), antiferroelectric splay crystal ($Cr_S P_A$), antiferroelectric double-splay crystal ($Cr_{DS}P_A$), and ferroelectric double-splay crystal ($Cr_{DS}P_F$). The phase diagram is presented in Fig. 2, the order parameters are shown in Fig. 3, while Figs. 4–6 contain correlation functions. Moreover, representative equilibrium snapshots of all phases can be seen in Figs. 8 and 9. The phases for all sampled pairs (d, η) were manually classified using order parameters and visual
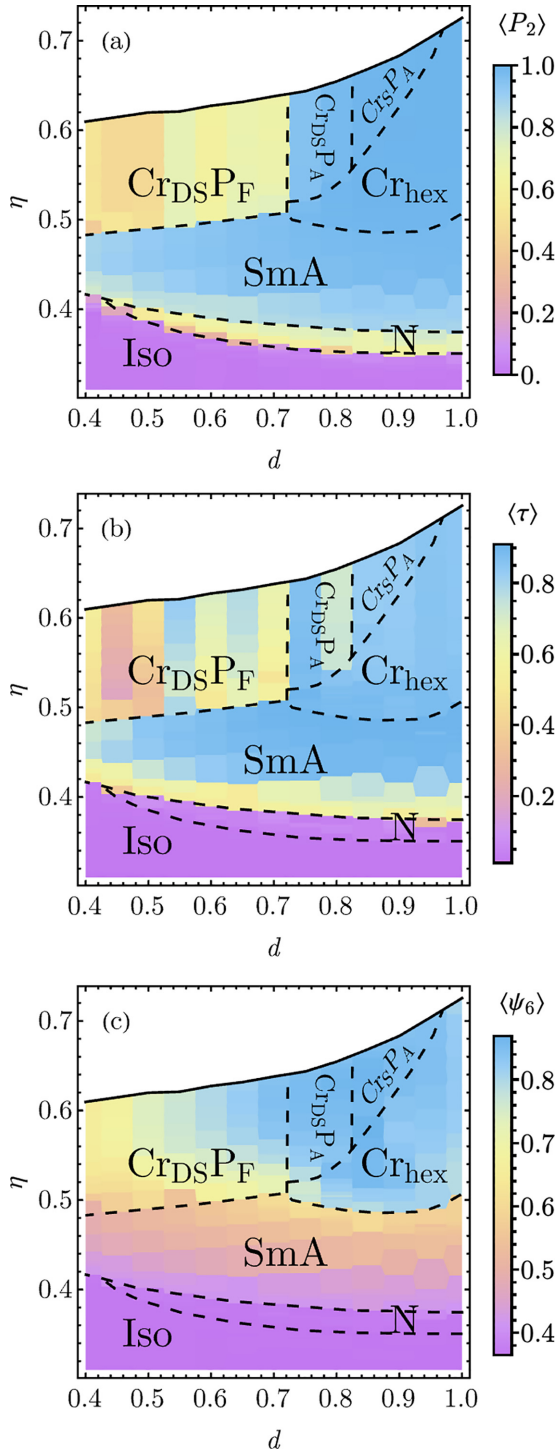
FIG. 3. Ensemble averages of observables as a function of the smallest sphere's diameter d and packing fraction η. (a) Nematic order $\langle P_2 \rangle$, (b) smectic order $\langle \tau \rangle$, and (c) local hexatic order $\langle \psi_6 \rangle$.

inspection of system snapshots. They are thoroughly analyzed in the following sections.

A. Liquid phases

For the lowest packing densities η, the system forms an isotropic liquid phase without any long-range translational or
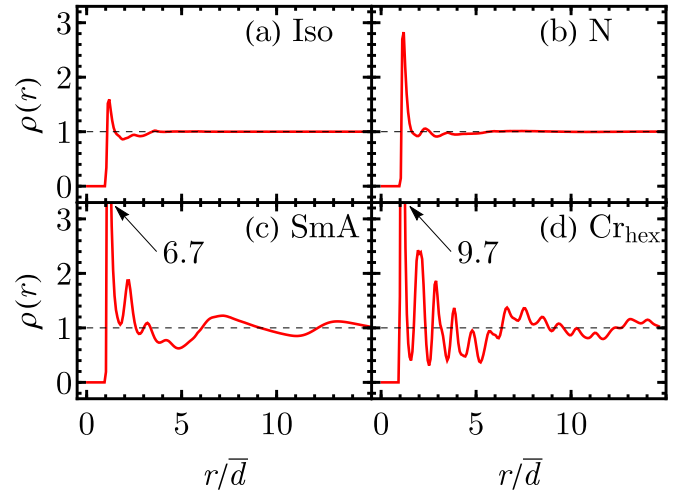

FIG. 4. Radial distribution function $\rho(r)$ for (a) Iso [$(d, \eta) = (0.6, 0.34)$], (b) N [$(d, \eta) = (0.5, 0.39)$], (c) SmA [$(d, \eta) = (0.5, 0.46)$], and (d) Cr_{hex} [$(d, \eta) = (0.95, 0.51)$] phases. Distance r is scaled by the average diameter of balls in the molecule: $\bar{d} = (d + 1)/2$. Correlation peaks are clipped on panels (c) and (d); however, their values are shown inside the plots.

orientational ordering. An example snapshot of this phase is shown in Fig. 8(a). In this phase, the values of the nematic order parameter $\langle P_2 \rangle$ and smectic order parameter $\langle \tau \rangle$ are close to zero, indicating the absence of alignment or layering. The hexatic order parameter $\langle \psi_6 \rangle$ also has a minimal value (see Fig. 3), indicating a lack of hexagonal arrangement. The radial distribution function [Fig. 4(a)] shows only local correlations, which disappear for distances $r/\bar{d} > 4$, where $\bar{d} = (1 + d)/2$ is the average diameter of balls that build the molecule. The maxima and minima are around integer multiples of $\bar{d}$: $r/\bar{d} = 1, 2, \ldots$, which can be attributed to the excluded volume effects.

Upon compression, in the range of $d \in [0.5, 1]$ the nematic phase appears stable [see Fig. 8(b)]. In this phase, the molecules orient, on average, along a preferred direction called the director $\hat{\mathbf{n}}$, while maintaining liquidlike positions of their centers of mass. The nematic order parameter $\langle P_2 \rangle$ exhibits a sharp increase at the phase boundary, jumping from 0 to 0.5–0.6 [Fig. 3(a)]. The smectic order parameter $\langle \tau \rangle$ and the hexatic order parameter $\langle \psi_6 \rangle$, however, remain nearly minimal [Figs. 3(b) and 3(c)]. The range of the nematic phase in terms of packing fraction ($\Delta\eta$) is approximately $\Delta\eta \approx 0.03$ for all d, but it drops to zero for the lowest values of d. The Iso-N phase boundary reaches a minimal value of η at around $\eta \approx 0.35$ for the highest value of d and then moves upward towards a triple point $(d, \eta) = (0.5, 0.4)$ as d decreases.

It is expected that as the value of d decreases, the molecules become shorter (less anisotropic). Consequently, a higher pressure is needed to induce ordering in the system. As η increases, the nematic order parameter $\langle P_2 \rangle$ reaches values of 0.6–0.8. These values are relatively high compared to the typical range observed in experiments [0.3, 0.7] [53]. However, they are comparable to values reported in computational studies of other hard-shaped molecules [18,38,54].
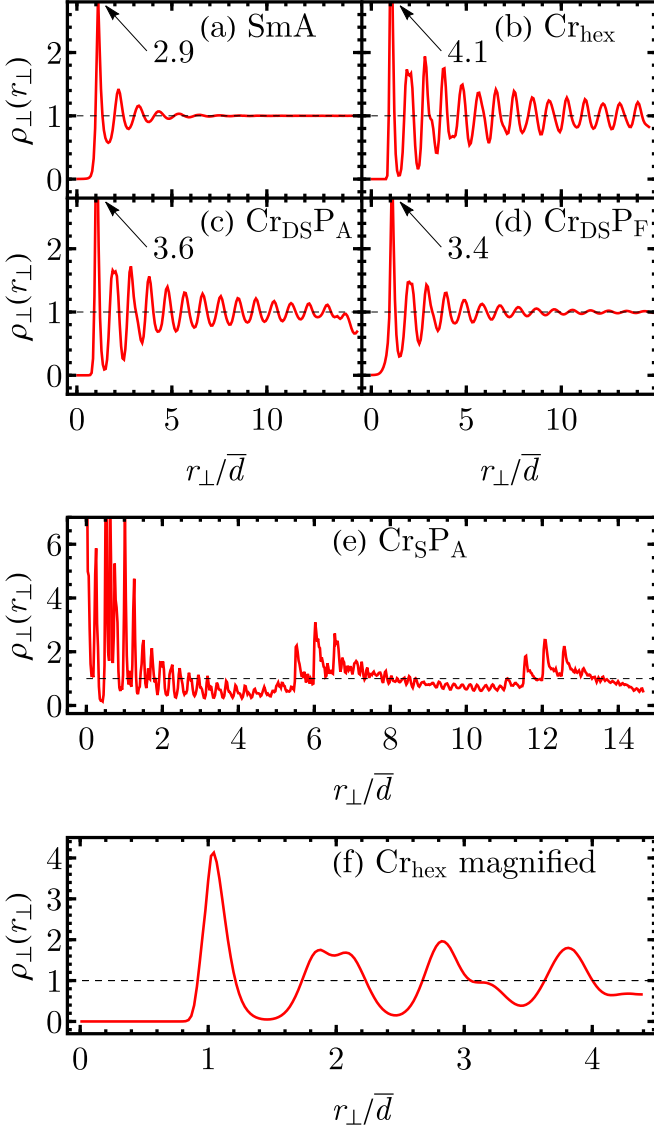
FIG. 5. Layerwise distribution function $\rho_\perp(r_\perp)$ for (a) SmA $[(d, \eta) = (0.5, 0.46)]$, (b) Cr_hex $[(d, \eta) = (0.95, 0.51)]$, (c) $\text{Cr}_\text{DS}\text{P}_\text{A}$ $[(d, \eta) = (0.75, 0.52)]$, (d) $\text{Cr}_\text{DS}\text{P}_\text{F}$ $[(d, \eta) = (0.6, 0.51)]$, and (e) $\text{Cr}_\text{S}\text{P}_\text{A}$ $[(d, \eta) = (0.9, 0.68)]$ phases. (f) Magnification of a part of panel (b). Distance $r_\perp$ is scaled by the average diameter of balls in the molecule: $\bar{d} = (d + 1)/2$. Correlation peaks are clipped on panels (b), (c), and (d); however, their values are shown inside the plots.

The radial distribution function $\rho(r)$ [Fig. 4(b)] exhibits a series of maxima and minima around $r/\bar{d} = 1, 2, \ldots$, which is typical for liquids [42]. However, compared to the Iso phase, the first maximum is more than two times higher, indicating stronger correlations. These correlations diminish at larger distances, for $r/\bar{d} > 6$.

In the ferroelectric nematic (N_F) and splay nematic (N_S) phases, a long-range polarization order is present. Thus, it is imperative to quantify it in our system. Although layers are not present in the nematic phase, it is still possible to compute $S_\perp^{110}(r_\perp)$. The simplest solution would be to project all molecules onto a single plane. However, in order to facilitate capturing local correlations, we divided the box into six iden-
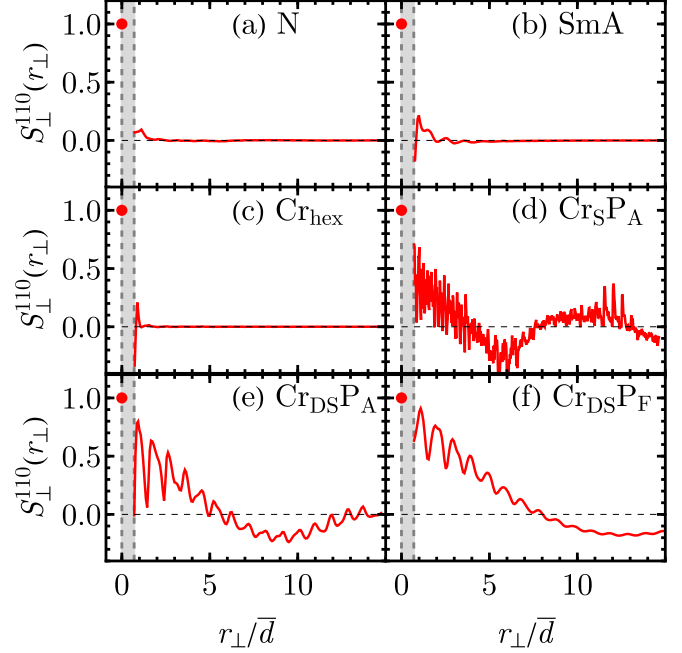

FIG. 6. Layerwise correlation function $S_\perp^{110}(r_\perp)$ for (a) N $[(d, \eta) = (0.5, 0.34)]$, (b) SmA $[(d, \eta) = (0.5, 0.46)]$, (c) Cr_hex $[(d, \eta) = (0.95, 0.51)]$, (d) $\text{Cr}_\text{S}\text{P}_\text{A}$ $[(d, \eta) = (0.9, 0.68)]$, (e) $\text{Cr}_\text{DS}\text{P}_\text{A}$ $[(d, \eta) = (0.75, 0.52)]$, and (f) $\text{Cr}_\text{DS}\text{P}_\text{F}$ $[(d, \eta) = (0.6, 0.51)]$ phases. Distance $r_\perp$ is scaled by the average diameter of balls in the molecule: $\bar{d} = (d + 1)/2$. Due to excluded volume, there are scarcely any molecules in range $r_\perp \in [0, \bar{d}]$; therefore, this area is grayed out.

tical slices (consistent with the number of layers in smectic and crystalline phase) and proceeded to compute $S_\perp^{110}(r_\perp)$ as it would be done for layered structures. The results are presented in Fig. 6(a). It is evident that the polarization correlations are relatively weak and short ranged, vanishing completely for $r_\perp > 2\bar{d}$. Similarly, the splay correlations [Fig. 7(a)] also exhibit a local range. The most probable angle in the system is approximately $\theta \approx 25°$, although the maximum has a broad distribution.

The type-A smectic phase (SmA) is formed over the Iso phase for $r \in [0.4, 0.5]$ and over the N phase for $r \in [0.5, 1.0]$. This phase is characterized by a significant jump in the smectic order parameter $\langle\tau\rangle$ [Fig. 3(b)] to around 0.5, indicating the emergence of well-defined layers [as seen in the snapshot from Fig. 8(c)]. The director $\hat{\mathbf{n}}$ is parallel to the smectic wave vector $\mathbf{k}$, indicating the preferred orientation of the molecules within the layers.

In the SmA phase, there is a slight increase in the value of the parameter $\langle\psi_6\rangle$ compared to the isotropic and nematic phases, ranging from 0.38 to 0.45. In the high packing fraction regime of this phase, $\langle\psi_6\rangle$ reaches values of 0.6–0.65, indicating some degree of local hexatic ordering within the layers. However, it is important to note that long-range bond order is not present in this phase [55], distinguishing it from other smectic phases such as type-B smectic [56]. The nematic order parameter $\langle P_2\rangle$ in SmA increases with increasing η, approaching a value close to 1. However, there is no sudden jump in $\langle P_2\rangle$ at the N-SmA boundary. Similar to the N phase,
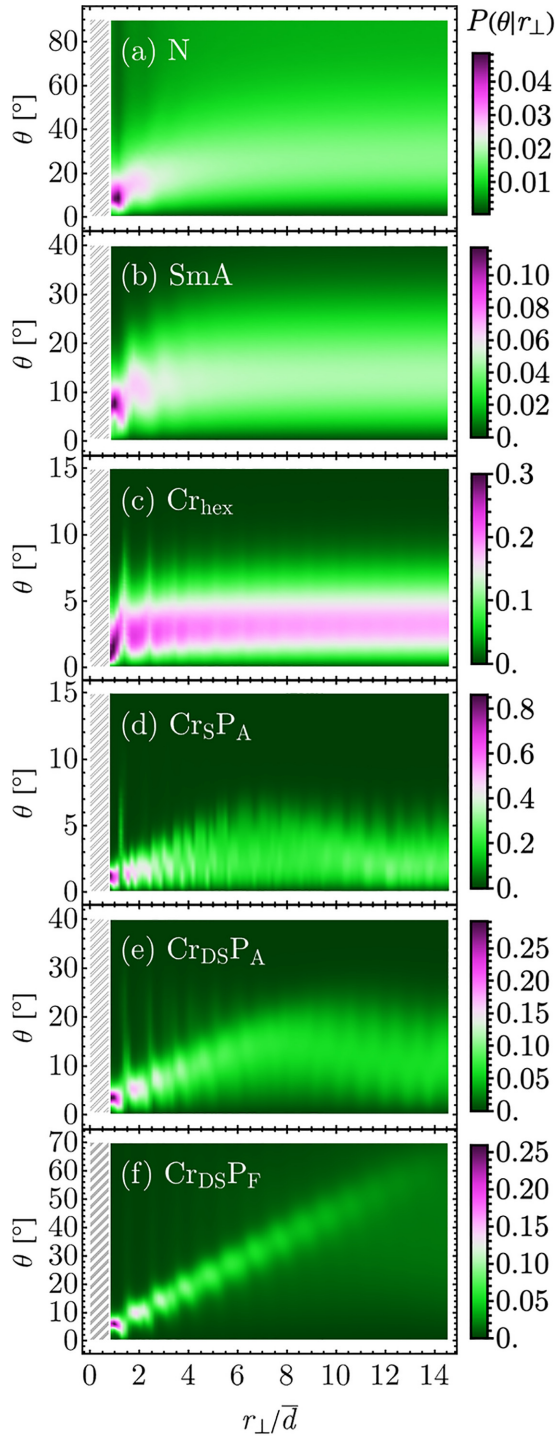
FIG. 7. The conditional probability $P(\theta|r_\perp)$ for (a) N [$(d, \eta) = (0.5, 0.34)$], (b) SmA [$(d, \eta) = (0.5, 0.46)$], (c) Cr_{hex} [$(d, \eta) = (0.95, 0.51)$], (d) $Cr_S P_A$ [$(d, \eta) = (0.9, 0.68)$] (e) $Cr_{DS} P_A$ [$(d, \eta) = (0.75, 0.52)$], and (f) $Cr_{DS} P_F$ [$(d, \eta) = (0.6, 0.51)$] phases.

the boundary moves upward with decreasing d, which can again be explained by a lower anisotropy of the molecules.

The radial distribution function $\rho(r)$ [see Fig. 4(c)] in SmA exhibits a more complex structure compared to the Iso and N phases. It shows two superimposed sequences of minima and maxima. The first sequence, covering the entire range of

$r/\bar{d}$, exhibits maxima at $r/\bar{d} \approx 7$ and 14, corresponding to the distances between the layers. The second sequence has a spacing of approximately $\bar{d}$ and vanishes for $r/\bar{d} > 6$. The first maximum in the second sequence is sharp and has a value of $\rho(r) = 6.7$, corresponding to short-range ordering of molecules within the layers.

The layerwise distribution function $\rho_\perp(r_\perp)$ [Fig. 5(a)] confirms the local translational order within the layers. It shows maxima at $r_\perp/\bar{d} = 1, 2, \ldots$, indicating correlations between molecules within the same layer. However, these correlations phase out for $r_\perp/\bar{d} > 9$, indicating that the translational order is only local within the layers.

The correlation function $S_\perp^{110}(r_\perp)$ [Fig. 6(b)] shows no long-range correlation of molecular polarization vectors in SmA. For $r_\perp/\bar{d} \approx 1$ a slight anticorrelation [$S_\perp^{110}(r_\perp) < 0$] is visible due to entropic reasons, where nearest-neighbor molecules tend to orient in opposite ways to increase packing density. However, these correlations vanish for $r_\perp/\bar{d} > 4$. Similarly, the splay correlations [Fig. 7(b)] remain only local within the smectic-A phase. The preferred angle for splay correlations is lower ($\theta \approx 12°$) compared to the N phase, and the spread of angles is also lower, which is consistent with the higher value of the nematic order parameter $\langle P_2 \rangle$ in the smectic phase.

Both sequences of phase transitions displayed by the system, (1) Iso $\leftrightarrow$ N $\leftrightarrow$ SmA and (2) Iso $\leftrightarrow$ SmA, are prominent and well recognized in systems of elongated molecules, both in computational studies [17,18,38,54], and in experiments [57–59], although the second sequence is less common in physical systems.

For asymmetric molecules, modulated and/or polar liquid crystalline phases may form (see the Introduction section). However, in our model, such phases were not observed. The absence of ferroelectric long-range order, even in the metastable regime, is further confirmed by bifurcation analysis using Parsons-Lee density functional theory (see Sec. IV). Two possible reasons for this absence can be considered: the first one is the moderate length of the molecule, which may hinder the formation of long-range ferroelectric-like order, and the second one is the concavities between the beads in the molecular structure. We, however, note that preliminary studies of analogous systems of taper-shaped molecules built of up to 11 beads as well as ones with the smooth, convex surface show no considerable change in the predictions presented by the current study.

B. Crystalline phases

Over $\eta \approx 0.5$, four distinct types of hexagonally ordered solids that retain the SmA layered structure appear.

1. Hexagonal nonpolar crystal Cr_hex

For $d \in [0.75, 1.0]$, SmA is adjacent to a hexagonal nonpolar crystal phase denoted Cr_{hex}, whose snapshot is shown in Fig. 9(a). Both $\langle P_2 \rangle$ and $\langle \tau \rangle$ are almost equal to 1 in the entire range, as seen in Figs. 3(a) and 3(b). Additionally, there is a sharp jump in the local hexatic order parameter, as depicted in Fig. 3(c), confirming the presence of a locally hexatic structure within a layer. The long-range translational order becomes apparent when observing the radial and layerwise
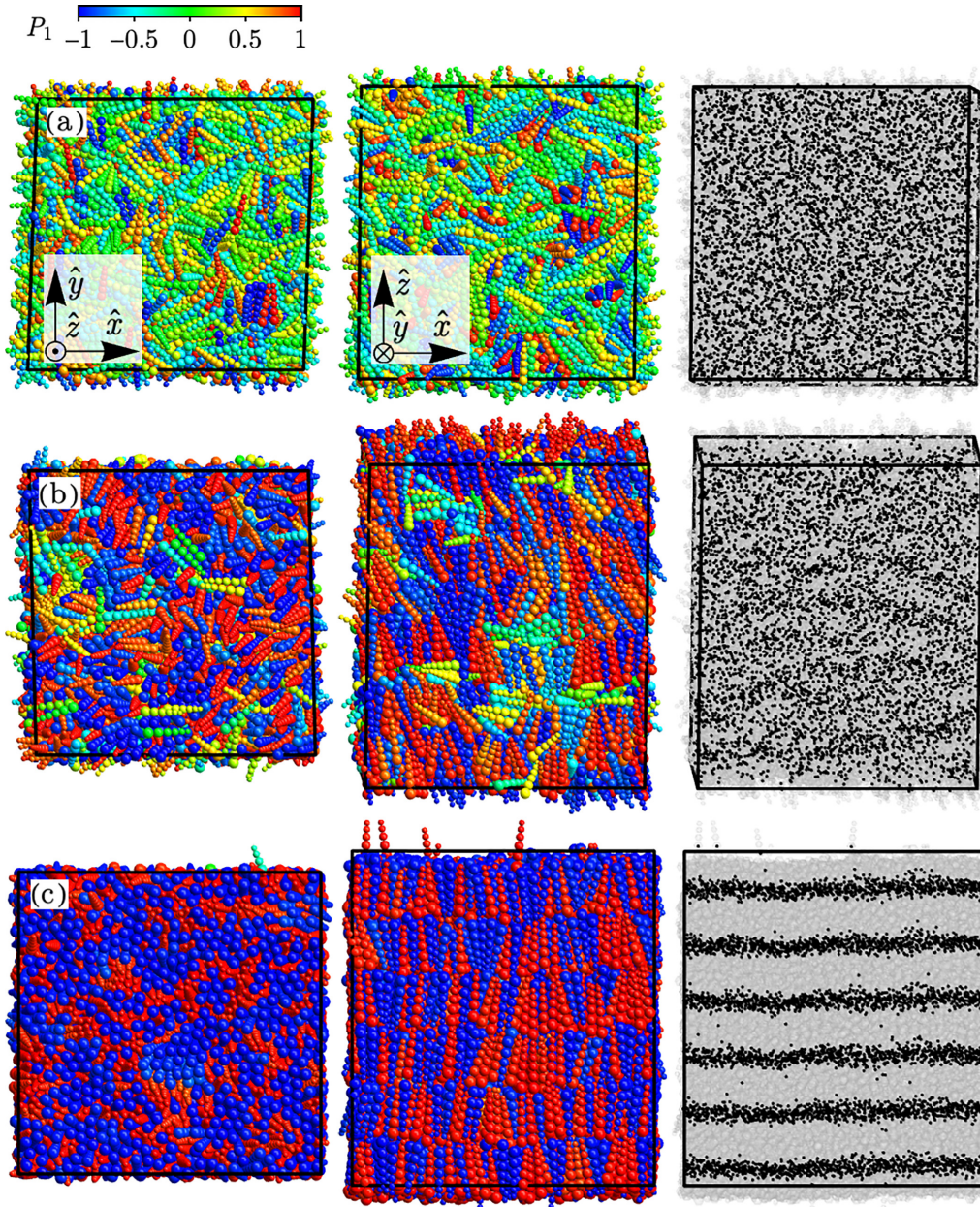
FIG. 8. System snapshots of all liquid phases in the system. Rows correspond to (a) Iso [$(d, \eta) = (0.6, 0.34)$], (b) N [$(d, \eta) = (0.5, 0.39)$], and (c) SmA [$(d, \eta) = (0.5, 0.46)$] phases. The first column presents the top view of the snapshot (xy plane), and the second one the side view (xz) plane in a way that the bottom edge of the top view corresponds to the top edge of the side view. Molecules are color coded according to orientation of their long axis $\hat{\mathbf{a}}_i$ with respect to the global director $\hat{\mathbf{n}}$ as per first-order Legendre polynomial $P_1(\hat{\mathbf{a}}_i \cdot \hat{\mathbf{n}}) = \hat{\mathbf{a}}_i \cdot \hat{\mathbf{n}}$, allowing one to discern opposite polarizations. In the third column midpoints of molecules' lengths are marked as black dots, and the simulation box is oriented in the same way as the second column (side view).

pair distribution functions $\rho(r)$ and $\rho_\perp(r_\perp)$, respectively, as shown in Figs. 4(d) and 5(b). In the case of $\rho(r)$, we observe two sequences of maxima. Similar to SmA, the first sequence with larger spacing corresponds to layering, while the second sequence with a smaller peak-to-peak distance corresponds to in-layer order. However, unlike SmA, the second sequence does not vanish quickly and extends throughout the entire plotted range of $r/\bar{d}$. Similarly, $\rho_\perp(r_\perp)$ also exhibits long-range correlations. Additionally, the structure of the first few peaks of $\rho_\perp(r_\perp)$, as shown in Fig. 5(f), agrees with the one observed for the hexagonal honeycomb lattice (see, e.g., Fig. 3 of

Ref. [60]). The $S_\perp^{110}(r_\perp)$ correlations, as depicted in Fig. 6(c), indicate weak and extremely short-range polarization order, which disappears for $r_\perp/\bar{d} > 2$. A similar observation can be made for the splay correlations shown in Fig. 7(c), where the preferred angle is close to $0°$ with a very narrow spread. The presence of a series of additional vertical lines is possibly a result of lattice defects.

For $d = 1$, the taper reduces to a well-known linear tangent hard-sphere (LTHS) hexamer. The equilibrium phases in the LTHS model have been studied in Ref. [38]. The ground-state configuration in this case is a close-packed arrangement of
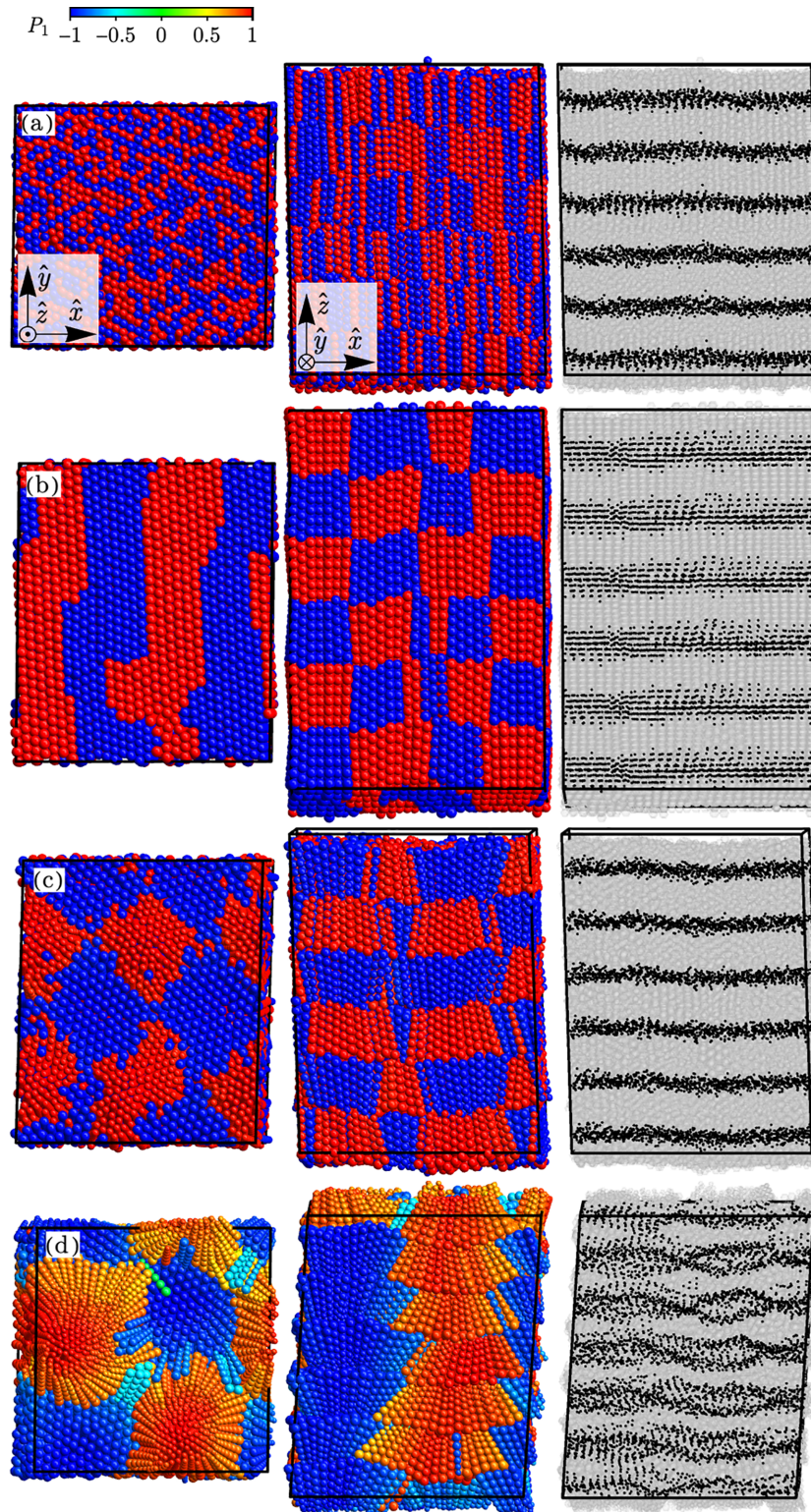
FIG. 9. System snapshots of all crystalline phases in the system. Rows correspond to, respectively, (a) Cr_{hcp} [$(d, \eta) = (0.95, 0.51)$], (b) $Cr_S P_A$ [$(d, \eta) = (0.9, 0.68)$], (c) $Cr_{DS} P_A$ [$(d, \eta) = (0.75, 0.52)$], and (d) $Cr_{DS} P_F$ [$(d, \eta) = (0.6, 0.51)$] phases. Columns' order and color coding are the same as in Fig. 8. From the left: top view, side view, and side view of molecules lengths' midpoints. The average number of molecules in clusters is as follows: (b) ≈ 7 per stripe per XZ section, (c) ≈ 110 per cluster, and (d) ≈ 220 per column per layer.

spheres [61], with a packing fraction of $\eta = \pi / \sqrt{18} \approx 0.74$. In our simulations, we were able to achieve a packing fraction of approximately $\eta \approx 0.73$ upon compression, which is in good agreement with the exact value, taking into account the presence of a small number of defects in the Monte Carlo configuration. There are various ways to arrange LTHS chains into a close-packed configuration. One obvious choice is to form face-centered cubic (fcc) or hexagonal close-packed

(hcp) layers of molecules with a $30°$ tilt (e.g., the CP_1 lattice in Ref. [62], also utilized in the previously mentioned Ref. [38]). However, these configurations are unlikely to form during the compression route from SmA layers.

More probable are nontilted variants with a partial hexatic order. We have identified two such structures referred to as fcc_B and hcp_B (see the Appendix). In these structures, six nearest neighbors within a layer form slightly deformed regular hexagons. This deformation is consistent with the values of $\langle \psi_6 \rangle$ below 0.8 for $d = 1$, compared to over 0.8 for $d = 0.85$. In the fcc_B and hcp_B lattices, the polymers arrange themselves into infinite columns that can be translated by integer multiples of the diameter $d = 1$ of the monomers. Our results exhibit a slight off-layer spread [observed in the last column of Fig. 9(a)], which also contributes to lowering the value of $\langle \tau \rangle$.

2. Antiferroelectric splay crystal Cr_SP_A

When d is decreased and the variation of bead diameters increases, the preference for a closed-packed configuration diminishes, and crystalline analogs of polar blue phases emerge. The first one is visible in a range around $d = 0.85$–0.95 (see Fig. 2). The corresponding snapshot is presented in Fig. 9(b). As clearly visible in the snapshot, within each layer, clusters with macroscopic polarization spontaneously emerge and arrange themselves in a striped metastructure. Adjacent clusters exhibit opposite polarization and are separated by planar defects in the polarization field.

Within a cluster, the molecules have a long-range translational order, which is indicated by the correlation function $\rho_\perp(r_\perp)$ [Fig. 5(e)] and they form a hexagonal structure, reflected in a high value of $\langle \psi_6 \rangle$ [Fig. 3(c)]. The density correlations exhibit a complex structure. First, there is a series of wide maxima and minima separated by $\Delta r_\perp \approx 6\bar{d}$, which corresponds to the width of the stripes. Around these wide maxima, there are three or four sharper ones separated by $\Delta r_\perp \approx \bar{d}$, representing correlations between particular rows of shapes across the stripes. Additionally, numerous small maxima represent correlations between individual beads in a highly regular lattice. However, this phase appears only for very high values of η close to the maximal packing. The macroscopic polarization of the cluster is confirmed by $S_\perp^{110}(r_\perp)$ correlations [see Fig. 6(d)]. Similarly, for $\rho_\perp(r_\perp)$, we observe minima and maxima, but with a twofold smaller separation, as the adjacent stripes have opposite polarizations. Furthermore, there is a similar series of additional maxima as observed in $\rho_\perp(r_\perp)$.

The nematic order $\langle P_2 \rangle$ remains above 0.8 but is slightly lower than for Cr_{hex}. This can be explained by the observation that clusters exhibit a splay modulation in the polarization field. Specifically, the polarization is parallel to the director in the middle of the stripe and gradually leans when one moves towards the boundary. However, the preferred direction does not change along the length of a stripe. This observation is supported by the $P(\theta|r_\perp)$ histogram [Fig. 7(d)], where, for the first time, a linear growth of the preferred angle θ with $r_\perp$ is observed until $r_\perp \approx 7\bar{d}$. After this point, a linear decline follows. The ascending part of the histogram corresponds to correlations within a single stripe, while the falling part corresponds to correlations between adjacent stripes.

The entropically promoted pure splay, inherently related to the shape of the taper, cannot be extended globally without introducing energetically expensive defects. The observed two-dimensional splay modulation serves as a solution to this difficulty (frustration), enabling a more efficient filling of space. Notably, the pattern of clusters in adjacent layers continues, but their polarization always has an opposite sign. The same sign reversal applies to the direction of splay modulation. Consequently, the stripes (y-axis columns) are arranged in a two-dimensional checkerboard pattern. The largest and smallest balls that form the molecules create hexagonal lattices with different lattice constants. The polarization switch in a neighboring layer facilitates a more compatible arrangement of adjacent layers.

The compatibility of lattice constants between adjacent beads can also be invoked to explain why molecules splay instead of forming an antiferroelectric interdigitated lattice, as observed in previous studies of pearlike shapes. When two adjacent tapers are antiparallel, the beads in contact have different radii, resulting in suboptimal local packing. In contrast, when the molecules are parallel, equally sized beads from adjacent molecules can be tangent, allowing them to form a nearly optimal local configuration.

To capture the most important properties of the structure, we refer to it as the *antiferroelectric splay crystal*, denoted as Cr_SP_A. The term *antiferroelectric* refers to the opposite polarization of the clusters in adjacent layers. It is worth noting that the Cr_SP_A phase emerges even when the value of d is close to 1. However, the phase boundary significantly increases as d grows. This behavior can be attributed to the requirement of higher densities to induce polar order when the gradient of ball diameters is smaller. In the entire range, the system first crystallizes into the Cr_{hex} structure, followed by a transition to the Cr_SP_A phase. Therefore, there is no direct SmA-Cr_SP_A phase transition present.

3. Antiferroelectric double-splay crystal $Cr_{DS}P_A$

Above Cr_{hex}, another polar phase is observed for $0.75 \leqslant d \leqslant 0.8$. The corresponding snapshot is shown in Fig. 9(c). In this phase, polarization clusters form again, but they arrange themselves within a layer in a checkerboard pattern instead of stripes. Each square domain is surrounded by four domains with opposite polarization. When moving to an adjacent layer, the polarizations of the clusters flip, similar to Cr_SP_A. This indicates that the checkerboard pattern is actually three dimensional.

The splay pattern also changes in this phase. It becomes three dimensional, where the direction of the splay vector $\hat{\mathbf{n}}(\nabla \cdot \hat{\mathbf{n}})$ is correlated with the polarization field. The molecules within the cluster are parallel to the z axis in the middle and gradually lean as the distance from the center increases. This structure is referred to as the *antiferroelectric double-splay crystal* ($Cr_{DS}P_A$). Importantly, the magnitude of the splay vector in the double-splay structure is higher compared to that in the single splay structure (assuming the same maximal curvature). This higher splay deformation is facilitated by molecules with smaller values of d, which

promotes a stronger modulation of the director field ultimately leading to the formation of the checkerboard pattern observed in $Cr_{DS}P_A$. It is also reflected in a slightly lower value of $\langle P_2 \rangle$ compared to $Cr_S P_A$.

In the $Cr_{DS}P_A$ phase, the transversal density correlation $\rho_\perp(r_\perp)$ [Fig. 5(c)] exhibits a similar behavior as in the Cr_{hex} [Fig. 5(b)], but with higher damping. The angle histogram $P(\theta|r_\perp)$ [Fig. 7(e)] in the $Cr_{DS}P_A$ phase is also similar to that in the $Cr_S P_A$ phase [Fig. 7(d)], but with larger preferred angles. Again, the difference is a result of stronger splay deformation in $Cr_{DS}P_A$ compared to $Cr_S P_A$. Regarding the polarization correlation function $S_\perp^{110}(r_\perp)$ [Fig. 6(e)], it shows positive correlations up to $r_\perp \approx 6.5\bar{d}$, and then negative correlations up to $r_\perp \approx 13\bar{d}$. This behavior is consistent with the snapshot in Fig. 9(c), where the cluster radius is estimated to be approximately six to seven times the average diameter of balls that build the molecule ($6\bar{d}$–$7\bar{d}$).

It is important to note that for a moderate number of molecules used in our study, the cluster radius may not be able to relax to its equilibrium value. The structure must adhere to periodic boundary conditions, which necessitates a single layer enclosing an even number of clusters. This requirement quantifies the surface area of the simulation box base. Simultaneously, the box height is constrained by the layer's width, and its volume is determined by the packing fraction. These parameters cannot be relaxed independently, even in a general triclinic simulation box. Consequently, the cluster radius is subject to systematic error. For a system in Fig. 9(c), the box accommodates eight clusters with a radius of approximately $6.5\bar{d}$. The two closest values are approximately $5.6\bar{d}$ and $7.3\bar{d}$, corresponding to six and ten clusters, respectively. Thus, the estimated uncertainty range of the radius can be approximated as $[(6.5 + 5.6)\bar{d}/2, (7.3 + 6.5)\bar{d}/2] \approx [6.0\bar{d}, 6.9\bar{d}]$. It is important to bear in mind that the slight nonequilibrium cluster radius can introduce frustration, potentially affecting other characteristic lengths, and consequently altering the uncertainty range. Finally, it should be noted that this issue did not arise in the two-dimensional $Cr_S P_A$ metastructure, where all structural dimensions could be relaxed independently.

4. Ferroelectric double-splay crystal $Cr_{DS}P_F$

For $d < 0.75$, the third frustrated polar structure, called the *ferroelectric double-splay crystal* ($Cr_{DS}P_F$), is formed directly above the SmA phase. Similar to $Cr_{DS}P_A$, the $Cr_{DS}P_F$ phase also exhibits the formation of polar clusters arranged in a checkerboard pattern [cf. Fig. 9(d)]. However, unlike $Cr_{DS}P_A$, where the clusters alternate between neighboring layers, in $Cr_{DS}P_F$ the clusters form vertical columns along the z axis that extend throughout the entire height of the simulation box.

The formation of these columns is accompanied by the bending of layers, as seen in the second and third panels of Fig. 9(d). Additionally, the decrease in the smectic order parameter $\langle \tau \rangle$ to the range 0.4–0.7 further indicates a curved layer structure. These curved layers cause the hexatic arrangement to deform when orthogonally projected, resulting in a lower hexatic order parameter $\langle \psi_6 \rangle$ in the range 0.65–0.75. The weaker nematic order $\langle P_2 \rangle$ in the range 0.5–0.8 is also consistent with the observed curved layers, which induce significant splay modulation.

Why is the $Cr_{DS}P_F$ structure stabilized for $d < 0.75$? For a simple explanation, please note that in $Cr_S P_A$ and $Cr_{DS}P_A$ the opposite interlayer polarization allows for the adjacency of compatible hexagonal bead lattices. However, this arrangement enforces flat layers, which becomes inefficient for smaller values of d. An efficient packing arrangement that leads to higher packing densities involves clusters that resemble fragments of a spherical shell. Achieving such an arrangement would require a ferroelectric alignment in the direction of the vector **k** to match the signs of curvatures. Interestingly, this is precisely what happens in the transition from $Cr_{DS}P_A$ to $Cr_{DS}P_F$. The formation of columns in $Cr_{DS}P_F$ allows for layer bending and the emergence of a mutually coupled ferroelectric arrangement in this phase. Although this ordering sacrifices the compatibility of the lattice constants of the beads, the packing microstructure remains similar to $Cr_{DS}P_A$.

There are long-range correlations observed in the transversal density correlation $\rho_\perp(r_\perp)$ [Fig. 5(d)], which, however, vanish faster than for $Cr_{DS}P_A$ or Cr_{hex}. This can be attributed to more irregular domain walls, which weaken the correlations between adjacent clusters. The polarization correlation function $S_\perp^{110}(r_\perp)$ [Fig. 6(f)] in $Cr_{DS}P_F$ is similar to that in $Cr_{DS}P_A$, and the cluster radius estimated at seven to eight molecule diameters agrees with a visual inspection of Fig. 9(d). The preferred angles on the angle histogram $P(\theta|r_\perp)$ [Fig. 7(f)] grow linearly with $r_\perp$, confirming the presence of long-range splay correlations. However, unlike in Figs. 7(d) and 7(e), a linear descent in the angle histogram is not observed in $Cr_{DS}P_F$.

Finally, with decreasing d the variation of ball diameters grows larger, which hinders the optimal filling of the space. As a result, the estimated maximal packing fraction η (see black solid line in Fig. 2) falls monotonically with d, reaching $\eta \approx 0.61$ for $d = 0.4$.

IV. DENSITY FUNCTIONAL ANALYSIS OF LIQUID CRYSTALLINE ORDER

Simulations show that the shape-induced splay deformations in the system of taper-shaped hard molecules can lead to unusually complex long-range orientational ordering in crystalline phases. What is somewhat unexpected is that the observed long-range orientational order in the liquid crystalline phases is not affected much. That is, only the ordinary uniaxial nematic and smectic-A phases are found at equilibrium. The question remains of whether liquid crystalline phases of non-nontrivial orientational ordering, such as e.g. ferroelectric nematic, ferroelectric smectic A, antiferroelectric smectic A, splay nematic or splay smectic, can form subject to purely steric interactions. Although we did not observe these in simulations as equilibrium states, it is imperative to assess whether such polar liquids are formed at least in a metastable regime. The simplest way to approach this issue is to perform density functional bifurcation analysis, in which the form of stable or metastable states can be selected at the start. In the following, we concentrate on the potential (meta)stability of ferroelectric nematic (N_F), smectic-A (SmA), and (anti)ferroelectric smectic-A (SmA_{AF}) phases using the second-virial density functional theory corrected by

the Parsons-Lee term (DFTPL) [63–65]. We will seek to gain a better understanding of the ability of taper-shaped molecules to form liquid phases with polar order. The study of the N-SmA bifurcation here serves as a reference.

The use of the DFTPL approach proved especially useful in the analysis of (meta)stable structures for hard molecules of complex shapes (see, e.g., Ref. [16]). We start with a brief summary of DFTPL for hard uniaxial molecules. More details can be found, e.g., in Refs. [16,66,67]. According to this theory, the Helmholtz free energy $\mathcal{F}$ of a system of N molecules in volume V at temperature T is a functional of the single-molecule probability density distribution function $P(X_i)$, where $X_i \equiv \{\mathbf{x}_i, \hat{\mathbf{a}}_i\}$ represents the position and orientation of the ith molecule. The distribution $P(X_i)$ is normalized so that

$$\text{Tr}_{(X_i)}P(X_i) = 1, \quad \text{Tr}_{(X_i)} = \int_V d^3\mathbf{r}_i \int d^2\hat{\mathbf{a}}. \quad (10)$$

After disregarding terms that can be made independent of P, the relevant part of the free energy per molecule for hard uniaxial molecules of arbitrary shape can be written as

$$f(P) \equiv \frac{\mathcal{F}[P]}{Nk_\text{B}T} = \text{Tr}_{(X)}[P(X)\ln P(X)]$$
$$+ C(\eta)\frac{\bar{\rho}}{2}\text{Tr}_{(X)}[P(X)H_\text{eff}(X,[P])] + \cdots, \quad (11)$$

where $\bar{\rho} = \frac{N}{V}$ is the average density. H_eff is the effective excluded volume averaged over the probability distribution of molecule "2" ($X \equiv X_1$):

$$H_\text{eff}(X_1, [P]) = V\text{Tr}_{(X_2)}\{\Theta[\xi(X_1, X_2) - r_{12}]P(X_2)\}, \quad (12)$$

where $\xi(\cdot)$ is the contact distance between two molecules, $\Theta(\cdot)$ is the Heaviside Θ function, and k_B is the Boltzmann constant. The factor $C(\eta) = (1/4)\frac{4-3\eta}{(1-\eta)^2}$ renormalizes the second-order virial expansion [63] to take into account the higher-order terms of the expansion [64,65]. Finally, r_{12} is the distance between two molecules, $\eta = \frac{v_\text{mol}N}{V} = v_\text{mol}\bar{\rho}$ is the packing fraction, and v_mol is the volume of a molecule.

The equilibrium states correspond to the minimum of the free energy functional, Eq. (11), with respect to $P(X)$, subject to the normalization condition, Eq. (10). The procedure is equivalent to solving the self-consistent integral equation for the stationary distributions $P_s(X)$:

$$P_s(X) = Z^{-1}\exp[-\bar{\rho}C(\eta)H_\text{eff}(X,[P_s])], \quad (13)$$

where

$$Z = \text{Tr}_{(X)}\exp[-\bar{\rho}C(\eta)H_\text{eff}(X,[P_s])] \quad (14)$$

and selecting the solution that minimizes the free energy (11) for a given set of control parameters. In general, for taper-shaped molecules, it is important to know whether they can stabilize states with some kind of polar order, such as polar nematics or smectics. The effective method for exploring this problem is the bifurcation analysis of Eq. (13) about the reference state, usually the isotropic or uniaxial nematic phase. Since tapers orient their steric dipole, on average, along the director $\hat{\mathbf{n}}(\mathbf{r})$, different local polar order of the predefined polarization profile $\hat{\mathbf{p}}(\mathbf{r})$ ($|\hat{\mathbf{p}}(\mathbf{r})| = 1$, $\hat{\mathbf{p}}(\mathbf{r}) = \pm\hat{\mathbf{n}}(\mathbf{r})$) can be tested against the instability of the reference state.

Here, we focus on bifurcation studies from the reference uniaxial nematic phase. As simulations show, the nematic order is high in both the uniaxial nematic and at the transition from the uniaxial nematic to higher-ordered phases (see Fig. 2), so we can further simplify the analysis by assuming that the orientational order is saturated. Consequently, the orientational degrees of freedom of the ith polar molecule can be described by a discrete pseudospin variable, $s_i = \pm 1$. It tells whether the steric molecular dipole is parallel ($s_i = 1$) or antiparallel ($s_i = -1$) to the preferred local orientational ordering, which is assumed to be positionally independent:

$$\mathbf{a}_i = s_i\hat{\mathbf{p}}. \quad (15)$$

In this case, the integration of orientational degrees of freedom is reduced to the sum over $s_i = \pm 1$, which means that

$$\text{Tr}_{(X_i)}[\cdots] = \text{Tr}_{(\mathbf{r}_i, s_i)}[\cdots] \equiv \text{Tr}_{(x_i, y_i, z_i, s_i)}[\cdots]$$
$$= \int_V d^3\mathbf{r}_i \sum_{s_i = \pm 1}(\cdots). \quad (16)$$

A more complex case of the nematic splay and smectic splay is left for an in-depth discussion elsewhere.

In practical calculations, we model the stationary distribution function $P_s \equiv P(\mathbf{r}, s) \equiv P(z, s)$ by expanding this to leading order in order parameters that describe the structures of interest. By limiting to nematic and smectic polar orderings of the constant $\hat{\mathbf{p}}$ (parallel to the z axis), this gives

$$P(z, s) = \frac{1}{V}\left[\frac{1}{2} + \frac{1}{2}\langle s\rangle s + \langle\cos\rangle\cos\left(\frac{2\pi z}{d'}\right)\right.$$
$$+ \langle\sin\rangle\sin\left(\frac{2\pi z}{d'}\right) + \langle s\cos\rangle s\cos\left(\frac{2\pi z}{d''}\right)$$
$$\left.+ \langle s\sin\rangle s\sin\left(\frac{2\pi z}{d''}\right) + \cdots\right], \quad (17)$$

where

$$\{\langle s\rangle, \langle\cos\rangle, \dots, \langle s\sin\rangle\}$$
$$= \text{Tr}_{(\mathbf{r}_i, s_i)}P(z, s)\left\{s, \cos\left(\frac{2\pi z}{d'}\right), \dots, s\sin\left(\frac{2\pi z}{d''}\right)\right\} \quad (18)$$

are the order parameters and where the length of the box ($V^{\frac{1}{3}}$) is assumed to be a multiple of the smectic periods d' and d''.

Note that in expansion, Eq. (17), the order parameter $\langle s\rangle$ represents the long-range polar order of the molecules in the nematic, smectic, and crystalline phases, while $\langle s\rangle\hat{\mathbf{p}}$ is the average polarization. In the case of SmA with density modulation along the z axis of the laboratory frame, only the order parameter $\langle\cos\rangle$ is not zero while d' is the period of the structure. This phase is always stable in simulations and will therefore serve as a test for bifurcation theory. The remaining order parameters can be combined to form antiferroelectric smectic phases, but detailed predictions depend on the solutions of Eq. (13).

The calculations can now proceed by pointing out that the order parameters are small near the bifurcation point. This

enables us to linearize Eq. (13) for a very small nonzero value of $\delta P(z,s)$, where $\delta P(z,s) = P(z,s) - P_0$; $P_0 = \frac{1}{2V}$ takes into account the probability distribution of the ideally oriented uniaxial nematic phase. The resulting linear homogeneous equation for $\delta P(z,s)$ is given by

$$\delta P(z_1, s_1) = -\eta\, C(\eta)\left(\frac{1}{2v_{\text{mol}}}\right)\text{Tr}_{(z,s_2)}[\Theta(z, s_1, s_2)\,\delta P(z + z_1, s_2)]. \tag{19}$$

Here $\Theta(z, s_1, s_2) = \text{Tr}_{(x_{12}, y_{12})}\Theta[\xi(\mathbf{r}_{12}, s_1, s_2) - r_{12}]$ ($z \equiv z_{12}$), and v_{mol} is the volume of the molecule.

Before identifying the phases that can bifurcate from N, we observe that the excluded interval $\Theta(z, s_1, s_2)$ has a particularly simple form in relation to the variables $\{s_1, s_2\}$. Specifically, observing the symmetry of $\Theta(z, s_1, s_2)$, $\Theta(z, -1, 1) = \Theta(-z, 1, -1)$ and $\Theta(z, -1, -1) = \Theta(z, 1, 1) = \Theta(-z, 1, 1)$, we can replace $\Theta(z, s_1, s_2)$ with the sum

$$\Theta(z, s_1, s_2) = \Theta_0(z) + s_1 s_2 \Theta_1(z) + (s_1 - s_2)\Theta_2(z), \tag{20}$$

where

$$\Theta_0(z) = \Theta_0(-z) = \tfrac{1}{4}[2\,\Theta(z, 1, 1) + \Theta(z, 1, -1) + \Theta(-z, 1, -1)], \tag{21}$$

$$\Theta_1(z) = \Theta_1(-z) = \tfrac{1}{4}[2\,\Theta(z, 1, 1) - \Theta(z, 1, -1) - \Theta(-z, 1, -1)], \tag{22}$$

and where

$$4\Theta_2(z) = -4\Theta_2(-z) = \Theta(z, 1, -1) - \Theta(-z, 1, -1). \tag{23}$$

It should be noted that the term proportional to $(s_1 + s_2)$ disappears due to the symmetries mentioned above of $\Theta(z, s_1, s_2)$.

Now, the homogeneous Eq. (19) can be solved for $\delta P(z_1, s_1)$, and the solutions are parametrized by the corresponding packing fraction $\eta = \eta_b$. More specifically, for $P(z, s)$ given by Eq. (17), Eq. (19) becomes reduced to a set of homogeneous equations for the order parameters. They are given by

$$\langle s \rangle = \langle s \rangle \psi(\eta_b)\, \Theta_{1,s}, \tag{24}$$

$$\begin{pmatrix} \langle \cos \rangle \\ \langle s \sin \rangle \end{pmatrix} = \psi(\eta_b)\begin{pmatrix} \Theta_{0,c}(d') & -\Theta_{2,s}(d'')\delta_{d',d''} \\ -\Theta_{2,s}(d'')\delta_{d',d''} & \Theta_{1,c}(d'') \end{pmatrix}\begin{pmatrix} \langle \cos \rangle \\ \langle s \sin \rangle \end{pmatrix},$$

$$\begin{pmatrix} \langle \sin \rangle \\ \langle s \cos \rangle \end{pmatrix} = \psi(\eta_b)\begin{pmatrix} \Theta_{0,c}(d') & \Theta_{2,s}(d'')\delta_{d',d''} \\ \Theta_{2,s}(d'')\delta_{d',d''} & \Theta_{1,c}(d'') \end{pmatrix}\begin{pmatrix} \langle \sin \rangle \\ \langle s \cos \rangle \end{pmatrix}, \tag{25}$$

where

$$\Theta_{1,s} = \int_{-l}^{l} \Theta_1(z)\,\mathrm{d}z,$$

$$\Theta_{0,c}(d') = \int_{l}^{l} \Theta_0(z)\cos\left(\frac{2\pi z}{d'}\right),$$

$$\Theta_{2,s}(d') = \int_{l}^{l} \Theta_2(z)\sin\left(\frac{2\pi z}{d'}\right),$$

$$\Theta_{1,c}(d'') = \int_{l}^{l} \Theta_1(z)\cos\left(\frac{2\pi z}{d''}\right), \tag{26}$$

and where $\psi = -\frac{2\pi}{v_{\text{mol}}}\eta C(\eta)$; l is the molecular length. We should add that with Wolfram *Mathematica* the formulas for the coefficients $\Theta_{\alpha,\beta}$ can be found exactly for rational diameters of the spheres.

A priori one expects four types of bifurcating states from Eq. (25). The first is the ferroelectric phase (F), where only $\langle s \rangle$ becomes nonzero at η_b. Due to the symmetry of the reference state P_0 and of the excluded interval, Eq. (20), first-order bifurcation analysis does not lead to a coupling between $\langle s \rangle$ and the smectic or crystalline order. Thus, if any F results from Eq. (25), it cannot be fully identified and can actually correspond to a ferroelectric order of a nematic, smectic, or

crystal phase. To resolve which of the cases applies, a higher-order bifurcation analysis is needed in this case. For $d' \neq d''$ we expect classical smectic A (SmA) phase with nonzero $\langle \cos \rangle$ (equivalently $\langle \sin \rangle \neq 0$) and antiferroelectric smectic A (SmA$_{\text{AF}}$) phase where $\langle s \cos \rangle \neq 0$ (equivalently $\langle s \sin \rangle \neq 0$). The final possibility is where $d' = d''$. In this case, we expect the SmA$_d$ phase, where $\langle \cos \rangle \neq 0$ and $\langle s \sin \rangle \neq 0$, (equivalently $\langle \sin \rangle \neq 0$ and $\langle s \cos \rangle \neq 0$). The phase would be similar to SmA, but with d' incommensurate with l. As two order parameters condense at the bifurcation to SmA$_d$ the corresponding phase transition should generally be of first order.

The structure to stabilize as a result of the phase transition from uniaxial nematic is usually (but not always) the one that leads to the minimum value of η_b. In the case of smectics, the bifurcation packing fraction η_b also depends on d', which requires additional minimization of η_b with respect to the smectic period. The hierarchy of η_bs gives an idea of possible (meta)stable states that the model can predict.

We begin our detailed analysis by determining whether any type of long-range polar order can occur in our model. The solution $\langle s \rangle \neq 0$ bifurcates from N at η_b satisfying the equation [see Eq. (24)]

$$1 = \psi(\eta_b)\, \Theta_{1,s}. \tag{27}$$

Only the solution with $\eta_b > 0$, where η_b is smaller than the maximal packing fraction, corresponds to a physically acceptable ferroelectric state. Clearly, it satisfies the integral equation (13) for $\eta > \eta_b$. Note that for $\Theta_{1,s} > 0$ no physical solution of Eq. (27) for η_b exists. In this case, the excluded volume of the parallel arrangement of the steric dipoles prevails over that of the antiferroelectric one, suggesting that the preferred local ordering should be of an antiferroelectric type. The calculations reveal that for all d parameters studied, the bifurcating packing fraction is always negative ($\eta_b < 0$), which means that the ferroelectric polar order is globally unstable at the expense of some kind of antiferroelectric ordering. Interestingly, the same conclusions can be drawn for model molecules composed of one sphere of diameter 1 and five spheres with their diameter chosen at random between 1 and 0.4. We have checked this for a sample of about 10 000 different molecules. Overall, these results suggest that, within the assumptions and simplifications adopted, the density functional theory does not predict the existence of global polar ordering in the hard model systems built out of six spheres.

A similar analysis can be performed to study the bifurcation to SmA and SmA$_{AF}$. Here, the bifurcation equations ($d' \neq d''$), analogous to Eq. (27), are given by

$$1 = \psi(\eta_b)\,\Theta_{0,c}(d') \quad \text{for N-SmA,} \tag{28}$$

$$1 = \psi(\eta_b)\,\Theta_{1,c}(d'') \quad \text{for N-SmA}_{AF}. \tag{29}$$

A more complex case of SmA$_d$ ($d' = d''$) requires diagonalization of the symmetric 2×2 matrix

$$\begin{pmatrix} \Theta_{0,c}(d') & \Theta_{2,s}(d') \\ \Theta_{2,s}(d') & \Theta_{1,c}(d') \end{pmatrix}. \tag{30}$$

It allows us to reduce the matrix equations in Eq. (25) to independent linear equations. For example, taking the first of Eqs. (25) we obtain two independent linear relations similar to Eq. (24), where $\Theta_{1,s}$ is replaced by one of the eigenvalues of the matrix, Eq. (30), and $\langle s \rangle$ by a linear combination of order parameters, $\langle \cos \rangle + \frac{o_{12}}{o_{11}}\langle s \sin \rangle$; o_{ij}s are elements of the orthogonal matrix $\mathbf{o}$ that brings Eq. (30) into the diagonal form. By inspecting Eqs. (25) and (30) we find that in our case the corresponding bifurcation equation along with the bifurcating state becomes

$$\frac{2}{\psi(\eta_b)} = \Theta_{0,c} + \Theta_{1,c} - \sqrt{4\Theta_{2,s}^2 + (\Theta_{0,c} - \Theta_{1,c})^2} \tag{31}$$

$$\frac{\delta P(z,s)}{\varepsilon} = \langle \cos \rangle + \frac{2\Theta_{2,s}}{\Theta_{1,c} - \Theta_{0,c} + \sqrt{4\Theta_{2,s}^2 + (\Theta_{0,c} - \Theta_{1,c})^2}}$$
$$\langle s \sin \rangle, \tag{32}$$

where ε is an arbitrary parameter. As previously, the physical solution is one that leads to a minimum of $\eta_b > 0$ with respect to d'.

In Fig. 10 shown are η_bs found by numerically solving Eqs. (28), (29), and (31). Out of the assumed model structures, the one that bifurcates first is SmA$_d$ (continuous orange line in Fig. 10). It differs from SmA (black line in Fig. 10), characterized by $\langle \cos \rangle$, by the presence of the extra term $\frac{o_{12}}{o_{11}}\langle s \sin \rangle$ that accounts for the polarization wave. However, the relative importance of this last term is of the order of 1% of the
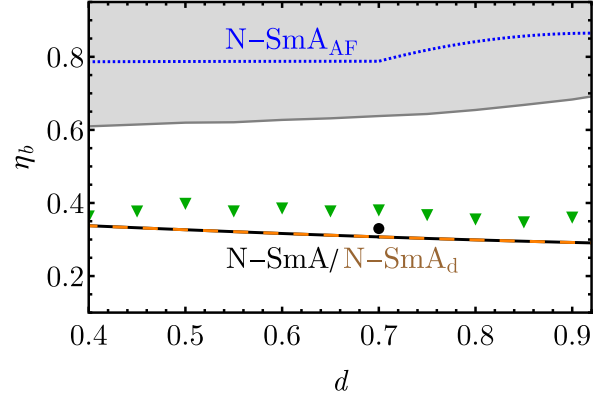

FIG. 10. Bifurcations from ideally oriented nematic phase. The black and orange dashed line denotes two practically overlapping N-SmA and N-SmA$_d$ bifurcation lines, the blue dotted line is the N-SmA$_{AF}$ bifurcation line, and the gray area is an inaccessible region of packing fractions above the optimal packing. Moreover, a black point is the N-SmA transition packing fraction $\eta \approx 0.33$ for $d = 0.7$ obtained from numerical simulation with axis-aligned molecules, while green triangles are N-SmA transition packing fractions from simulations without restricting molecule orientations (cf. Fig. 2).

leading smectic term. The reason for detecting only N-SmA in simulations is probably the nature of the N-SmA$_d$ transition, which should generally be first order due to the simultaneous condensation of two order parameters, unlike N-SmA. When comparing the simulation results with the N-SmA bifurcation, we find that the packing fraction of the bifurcation analysis is always lower than predicted by the simulations. This is due to the underestimation of the orientational entropy by the ideal nematic order, as opposed to the full spectrum of orientational degrees of freedom present in simulations. However, if an ideal nematic order is also assumed in the simulations, a very good agreement between simulation and theory for N-SmA is obtained (black dot shown in Fig. 10). A good agreement is obtained from simulations without restricting molecule orientations (green triangles shown in Fig. 10). A similar analysis for N-SmA$_{AF}$ shows that η_b is generally of the order of 0.8, which exceeds the physically accessible packing fractions for our systems.

V. SUMMARY AND FINAL COMMENTS

One of the most significant discoveries in the field of liquid crystals in recent years is the identification of the ferroelectric nematic phase (N$_F$) and the nematic phase with periodic long-range splay order (N$_S$). These phases were initially observed in the RM734 molecular system. While several systems known to exhibit stable polar nematic phases already exist, the key features of molecular interactions responsible for their stability are still under intensive study. Based on observations of molecular self-organization in the RM734 system, two factors appear to play a crucial role in stabilizing these phases: the conelike symmetry of the elongated molecule and the notably large net axial dipole moment of the molecule, exceeding 10 Debye units.

This research represents a systematic effort to uncover the essential features of molecular self-organization that can be

attributed to molecular shape asymmetry, as represented by RM734. We concentrated on a molecular system comprising hard taper-shaped molecules constructed from tangent spheres, where the molecular symmetry is controlled by a parameter called d, representing the ratio between the smallest and largest diameters of the spheres. An analogous hard-sphere model was previously investigated by Greco and Ferrarini [16], as well as by some of us [18]. It involved modeling bend-core-like mesogens using hard crescentlike molecules composed of identical beads. Through purely entropic interactions, this model stabilized another remarkable nematogenic phase known as the twist-bend nematic phase. Our goal was to explore the type of long-range orientational order stabilized by molecular systems exhibiting similar molecular asymmetry to RM734. Similar to the work of Greco and Ferrarini [16] and our own work [18], we focused on examining the role that packing entropy can play in stabilizing such order.

Using Monte Carlo (MC) simulations, we computationally obtained and analyzed self-organization for hard taper-shaped molecules consisting of six tangent spheres. We simulated a wide range of packing densities, spanning from those observed in ordinary liquids to the maximum packing fractions achievable for a given value of d. These maximal packings are represented by continuous lines in Figs. 2 and 3.

More systematically, for packing fractions below $\eta \approx 0.5$, which correspond to the liquid phase, we observed isotropic (Iso), nematic (N), and smectic-A (SmA) phases, as expected for systems built with calamitic molecules. However, we did not observe any polar or splay nematic or smectic phases. This observation was further supported by density functional theory (DFT) calculations and remains valid even in the metastable regime. Moreover, the DFT study suggests that the polar nematic phase is unstable not only for our system but also for other similar systems composed of six tangent balls with a nonzero steric dipole. Our preliminary MC simulations also indicate that even for analogous molecules consisting of up to 11 tangent beads or molecules with a smooth taper surface, there are no significant changes in the predictions. The absence of sterically induced ferroelectric long-range order still persists in these systems.

While a polar smectic-A phase is theoretically possible, it would require unphysically high packing fractions, approximately $\eta \approx 0.8$. An intriguing theoretical prediction involves the potential stabilization of a bilayer smectic phase (SmA$_d$) at practically the same packing densities characterizing SmA. A similar mesophase was observed in simulations of single-site hard pears [33], but not in our simulations for taper-shaped molecules.

The most striking observation was the presence of complex orientational periodic superstructures, involving hundreds of molecules as depicted in Fig. 9, that couple to the underlying crystalline order of molecular centers at high packing fractions. We label these phases as crystalline polar blue phases. Specifically, for $\eta > 0.5$, the system crystallizes while retaining the layered structure of SmA. Entropically promoted splay, inherently related to the shape of the taper, competes here with the tendency of layers to stay flat. The efficient filling of space depends on the actual value of the parameter d.

For $d \geqslant 0.75$, when the molecule is not far from the linear tangent hard-sphere (LTHS) hexamer, SmA transforms into a standard nonpolar hexagonal crystal (Cr$_{hex}$). However, for all $0.75 \leqslant d < 1$, further compression produces two other crystalline phases with frustrated polar order and periodic splay modulation. For d values around 0.85–0.95 (see Fig. 2), the striped antiferroelectric splay crystal (Cr$_S$P$_A$) phase emerges. Within each layer, clusters with macroscopic polarization spontaneously form, but in the adjacent clusters, the polarization is of opposite sign. The clusters are separated by planar defects in the polarization field. For lower values of the d parameter ($0.75 \leqslant d \leqslant 0.8$), periodic polar stripes appear, arranged in a checkerboard mesostructure. This structure is referred to as the antiferroelectric double-splay crystal (Cr$_{DS}$P$_A$). Again, the alternating polarization pattern facilitates a more efficient molecular packing.

While the splay pattern, coupled with a slight layer deformation, also changes in these two phases, the stabilization of the third phase, called ferroelectric double-splay crystal (Cr$_{DS}$P$_F$), relies entirely on significant splay modulation, leading to strongly curved layers. In the Cr$_{DS}$P$_F$ phase, which is stabilized for $d < 0.75$ directly from SmA, the ferroelectrically polarized splayed clusters form long columns arranged in a checkerboard pattern.

To our knowledge, none of these phases have been previously reported, but theoretical arguments support the existence of related mesophases in a liquid crystalline domain [22,23]. Specifically, Rosseto and Selinger [23] employed the Oseen-Zocher-Frank free energy model, enhanced by the inclusion of flexoelectric coupling between splay and polar order aligned with the director. Additionally, they incorporated a standard Landau free energy expansion based on the polar order parameter. With their theory, they investigated the stability of long-range splay ordering within nematic systems. Their analysis involved evaluating the relative stability of two nematic phases characterized by one-dimensional (1D) and two-dimensional (2D) splay modulations of the director field, respectively. In the 1D case, the system exhibited alternating (infinite) domains of splay and polar order. At interfaces where opposing domains met, both the polar order and splay diminished to zero, resulting in a local director characterized by pure bend deformation. In the 2D case, the double-splay structure was arranged in a 2D checkerboard pattern of alternating polar and splay order. Similarly, along the interfaces, both the polar order and splay went to zero. Both phases were shown to have their range of stability on the phase diagram although the 1D region was fairly small.

Referring to our simulations, none of the predicted orientational splay orderings for nematics have been observed, even though the orientational order of Cr$_{DS}$P$_F$ resembles that of the nematic double-splay structure. The fundamental difference in orientational ordering becomes apparent at the interfaces. In our case, we observe domain walls, while for the double-splay nematics, the splay and polar orderings decrease to zero, and a pure bend deformation of the director emerges.

APPENDIX: NONTILTED HEXAGONAL CONFIGURATIONS IN A CLOSE PACKING OF LTHS POLYMERS

We want to establish how one can arrange LTHS polymers in a maximally packed manner, assuming that they form hexatic layers without a tilt (with long molecular axes perpendicular to the layers). A naïve approach would be to prepare hexagonal honeycomb layers and stack them as in the type-B crystal [69], which is observed in systems of spherocylinders [19,54]. However, this configuration is not maximally packed. Therefore, we need to relax two conditions: molecules can deviate slightly from the layers, and hexagons can be slightly deformed. We have identified two such configurations on the basis of the fcc and hcp lattices.

The first configuration is constructed from an fcc lattice of spheres [see Fig. 11(a)]. For polymers consisting of beads k with diameter d, the unit cell has dimensions $d \times d\sqrt{2} \times kd$, and it contains two molecules with geometric
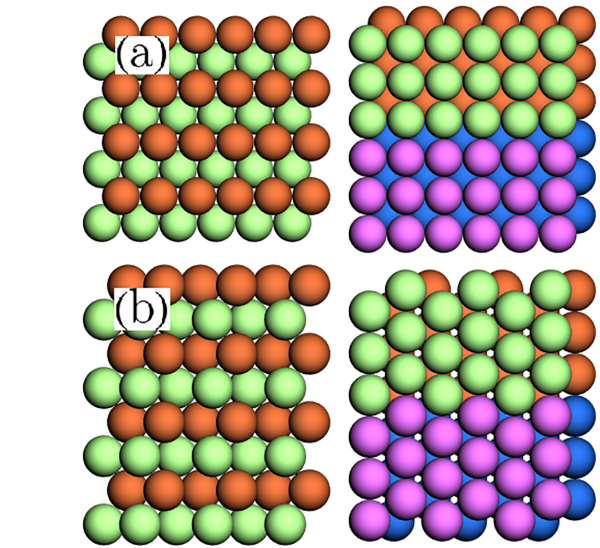

FIG. 11. (a) fcc_B and (b) hcp_B configurations of trimers ($k = 3$). First column is a top view with a visible deformed hexatic arrangement, while the second one is a side view. Colors are to visually separate the molecules.

centers: $(0, 0, kd/2 - d/4)$ and $(d/2, \sqrt{2}/2, kd/2 + d/4)$. We refer to this configuration as fcc_B.

The second configuration is based on the hcp lattice [see Fig. 11(b)]. The unit cell has dimensions $d\sqrt{3} \times 2d\sqrt{6}/3 \times kd$, and it contains four molecules with geometric centers: $(0, 0, kd/2 - d/4)$, $(d\sqrt{3}/3, d\sqrt{6}/3, kd/2 - d/4)$, $(d\sqrt{3}/2, 0, kd/2 + d/4)$, and $(5d/2\sqrt{3}, d\sqrt{6}/3, kd/2 + d/4)$. We refer to this structure as hcp_B.

---

[1] N. Sebastián, L. Cmok, R. J. Mandle, M. R. de la Fuente, I. Drevenšek Olenik, M. Čopič, and A. Mertelj, Ferroelectric-ferroelastic phase transition in a nematic liquid crystal, Phys. Rev. Lett. **124**, 037801 (2020).

[2] X. Chen, E. Korblova, D. Dong, X. Wei, R. Shao, L. Radzihovsky, M. A. Glaser, J. E. Maclennan, D. Bedrov, D. M. Walba *et al.*, First-principles experimental demonstration of ferroelectricity in a thermotropic nematic liquid crystal: Polar domains and striking electro-optics, Proc. Natl. Acad. Sci. USA **117**, 14021 (2020).

[3] R. J. Mandle, N. Sebastián, J. Martinez-Perdiguero, and A. Mertelj, On the molecular origins of the ferroelectric splay nematic phase, Nat. Commun. **12**, 4962 (2021).

[4] R. J. Mandle, A new order of liquids: Polar order in nematic liquid crystals, Soft Matter **18**, 5014 (2022).

[5] A. Mertelj, L. Cmok, N. Sebastián, R. J. Mandle, R. R. Parker, A. C. Whitwood, J. W. Goodby, and M. Čopič, Splay nematic phase, Phys. Rev. X **8**, 041025 (2018).

[6] M. Cestari, S. Diez-Berart, D. A. Dunmur, A. Ferrarini, M. R. de la Fuente, D. J. B. Jackson, D. O. Lopez, G. R. Luckhurst, M. A. Perez-Jubindo, R. M. Richardson, J. Salud, B. A. Timimi, and H. Zimmermann, Phase behavior and properties of the liquid-crystal dimer 1″, 7″-bis(4-cyanobiphenyl-4′-yl) heptane:

A twist-bend nematic liquid crystal, Phys. Rev. E **84**, 031704 (2011).

[7] V. Borshch, Y.-K. Kim, J. Xiang, M. Gao, A. Jákli, V. P. Panov, J. K. Vij, C. T. Imrie, M. G. Tamba, G. H. Mehl, and O. D. Lavrentovich, Nematic twist-bend phase with nanoscale modulation of molecular orientation, Nat. Commun. **4**, 2635 (2013).

[8] D. Chen, J. H. Porada, J. B. Hooper, A. Klittnick, Y. Shen, M. R. Tuchband, E. Korblova, D. Bedrov, D. M. Walba, M. A. Glaser, J. E. Maclennan, and N. A. Clark, Chiral heliconical ground state of nanoscale pitch in a nematic liquid crystal of achiral molecular dimers, Proc. Natl. Acad. Sci. USA **110**, 15931 (2013).

[9] C. W. Oseen, The theory of liquid crystals, Trans. Faraday Soc. **29**, 883 (1933).

[10] H. Zocher, The effect of a magnetic field on the nematic state, Trans. Faraday Soc. **29**, 945 (1933).

[11] F. C. Frank, I. Liquid crystals. On the theory of liquid crystals, Discuss. Faraday Soc. **25**, 19 (1958).

[12] R. B. Meyer, *Proceedings of the Les Houches Summer School on Theoretical Physics, XXV, 1973* (Gordon and Breach, New York, 1976).

[13] R. B. Meyer, Piezoelectric effects in liquid crystals, Phys. Rev. Lett. **22**, 918 (1969).

[14] A. Jákli, O. D. Lavrentovich, and J. V. Selinger, Physics of liquid crystals of bent-shaped molecules, Rev. Mod. Phys. **90**, 045004 (2018).

[15] I. Dozov, On the spontaneous symmetry breaking in the mesophases of achiral banana-shaped molecules, Europhys. Lett. **56**, 247 (2001).

[16] C. Greco and A. Ferrarini, Entropy-driven chiral order in a system of achiral bent particles, Phys. Rev. Lett. **115**, 147801 (2015).

[17] M. Chiappini and M. Dijkstra, A generalized density-modulated twist-splay-bend phase of banana-shaped particles, Nat. Commun. **12**, 2157 (2021).

[18] P. Kubala, W. Tomczyk, and M. Cieśla, In silico study of liquid crystalline phases formed by bent-shaped molecules with excluded volume type interactions, J. Mol. Liq. **367**, 120156 (2022).

[19] J. A. C. Veerman and D. Frenkel, Phase diagram of a system of hard spherocylinders by computer simulation, Phys. Rev. A **41**, 3237 (1990).

[20] D. Frenkel, B. M. Mulder, and J. P. McTague, Phase diagram of a system of hard ellipsoids, Phys. Rev. Lett. **52**, 287 (1984).

[21] P. De Gregorio, E. Frezza, C. Greco, and A. Ferrarini, Density functional theory of nematic elasticity: Softening from the polar order, Soft Matter **12**, 5188 (2016).

[22] S. M. Shamid, D. W. Allender, and J. V. Selinger, Predicting a polar analog of chiral blue phases in liquid crystals, Phys. Rev. Lett. **113**, 237801 (2014).

[23] M. P. Rosseto and J. V. Selinger, Theory of the splay nematic phase: Single versus double splay, Phys. Rev. E **101**, 052707 (2020).

[24] N. Sebastián, M. Čopič, and A. Mertelj, Ferroelectric nematic liquid crystalline phases, Phys. Rev. E **106**, 021001 (2022).

[25] X. Chen, V. Martinez, E. Korblova, G. Freychet, M. Zhernenkov, M. A. Glaser, C. Wang, C. Zhu, L. Radzihovsky, J. E. Maclennan *et al.*, The smectic Z_A phase: Antiferroelectric smectic order as a prelude to the ferroelectric nematic, Proc. Natl. Acad. Sci. USA **120**, e2217150120 (2023).

[26] J. Stelzer, R. Berardi, and C. Zannoni, Flexoelectric effects in liquid crystals formed by pear-shaped molecules. A computer simulation study, Chem. Phys. Lett. **299**, 9 (1999).

[27] J. Stelzer, R. Berardi, and C. Zannoni, Flexoelectric coefficients for model pear shaped molecules from Monte Carlo simulations, Mol. Cryst. Liq. Cryst. Sci. Technol. Sect. A **352**, 187 (2000).

[28] J. Gay and B. Berne, Modification of the overlap potential to mimic a linear site-site potential, J. Chem. Phys. **74**, 3316 (1981).

[29] R. Berardi, M. Ricci, and C. Zannoni, Ferroelectric nematic and smectic liquid crystals from tapered molecules, ChemPhysChem **2**, 443 (2001).

[30] M. Houssa, L. F. Rull, and J. M. Romero-Enrique, Bilayered smectic phase polymorphism in the dipolar Gay-Berne liquid crystal model, J. Chem. Phys. **130**, 154504 (2009).

[31] L. Longa, G. Cholewiak, and J. Stelzer, Structures and correlations in ideally aligned polar Gay-Berne systems, Acta Phys. Polon. B **31**, 801 (2000).

[32] L. Longa, H. Trebin, and G. Cholewiak, Computer simulations of polar liquid crystals, in *Relaxation Phenomena: Liquid Crystals, Magnetic Systems, Polymers, High-T_c Superconductors, Metallic Glasses* (Springer-Verlag, Berlin, 2003), pp. 204–235.

[33] F. Barmes, M. Ricci, C. Zannoni, and D. J. Cleaver, Computer simulations of hard pear-shaped particles, Phys. Rev. E **68**, 021708 (2003).

[34] L. J. Ellison, D. J. Michel, F. Barmes, and D. J. Cleaver, Entropy-driven formation of the gyroid cubic phase, Phys. Rev. Lett. **97**, 237801 (2006).

[35] P. W. Schönhöfer, L. J. Ellison, M. Marechal, D. J. Cleaver, and G. E. Schröder-Turk, Purely entropic self-assembly of the bicontinuous Ia3d gyroid phase in equilibrium hard-pear systems, Interface Focus **7**, 20160161 (2017).

[36] P. W. Schönhöfer, M. Marechal, D. J. Cleaver, and G. E. Schröder-Turk, Self-assembly and entropic effects in pear-shaped colloid systems. I. Shape sensitivity of bilayer phases in colloidal pear-shaped particle systems, J. Chem. Phys. **153**, 034903 (2020).

[37] T. Chen, Z. Zhang, and S. C. Glotzer, Simulation studies of the self-assembly of cone-shaped particles, Langmuir **23**, 6598 (2007).

[38] C. Vega, C. McBride, and L. G. Macdowell, Liquid crystal phase formation for the liner tangent hard sphere model from Monte Carlo simulations, J. Chem. Phys. **115**, 4203 (2001).

[39] E. R. Chen, D. Klotsa, M. Engel, P. F. Damasceno, and S. C. Glotzer, Complexity in surfaces of densest packings for families of polyhedra, Phys. Rev. X **4**, 011024 (2014).

[40] D. Klotsa, E. R. Chen, M. Engel, and S. C. Glotzer, Intermediate crystalline structures of colloids in shape space, Soft Matter **14**, 8692 (2018).

[41] E. G. Teich, G. van Anders, and S. C. Glotzer, Identity crisis in alchemical space drives the entropic colloidal glass transition, Nat. Commun. **10**, 64 (2019).

[42] M. P. Allen and D. J. Tildesley, *Computer Simulation of Liquids* (Oxford University Press, Oxford, UK, 2017).

[43] W. W. Wood, Monte Carlo studies of simple liquid models, in *Physics of Simple Liquids*, edited by H. N. V. Temperley, J. S. Rowlinson, and G. S. Rushbrooke (North-Holland, Amsterdam, 1968).

[44] W. Wood, Monte Carlo calculations for hard disks in the isothermal-isobaric ensemble, J. Chem. Phys. **48**, 415 (1968).

[45] A. Uhlherr, Parallel Monte Carlo simulations by asynchronous domain decomposition, Comput. Phys. Commun. **155**, 31 (2003).

[46] R. Eppenga and D. Frenkel, Monte Carlo study of the isotropic and nematic phases of infinitely thin hard platelets, Mol. Phys. **52**, 1303 (1984).

[47] P. G. de Gennes and J. Prost, *The Physics of Liquid Crystals*, 2nd ed. (Clarendon Press, Oxford, UK, 1993).

[48] $\mathbf{g}_i$ can be read off as rows of matrix $G = 2\pi \mathbf{M}^{-1}$, where columns of $\mathbf{M}$ are vectors spanning the simulation box.

[49] W. H. De Jeu, *Basic X-Ray Scattering for Soft Matter* (Oxford University Press, Oxford, UK, 2016).

[50] D. Nelson, *Bond-Orientational Order in Condensed Matter Systems* (Springer Science & Business Media, 2012).

[51] A. J. Stone, The description of bimolecular potentials, forces and torques: The S and V function expansions, Mol. Phys. **36**, 241 (1978).

[52] Please note that for general Miller indices *hkl* some layers may be connected through PBCs. n_L is a number of disjoint layers and is equal to the highest common divisor of h, k, l, while $S = V \| h\mathbf{g}_1 + k\mathbf{g}_2 + l\mathbf{g}_3 \|$.

[53] S. Chandrasekhar and N. V. Madhusudana, Liquid crystals, Annu. Rev. Mater. Sci. **10**, 133 (1980).

[54] S. C. McGrother, D. C. Williamson, and G. Jackson, A re-examination of the phase diagram of hard spherocylinders, J. Chem. Phys. **104**, 6755 (1996).

[55] Long-range bond order can be quantified using the global bond order parameter, where the modulus is on the outside of the outer $\sum_{i=1}^{N}$ sum [cf. Eq. (5)]; it is nonzero if local hexagons are in phase, which is not the case in our system (result not shown).

[56] R. Birgeneau and J. Litster, Bond orientational order model for smectic B liquid crystals, J. Phys. Lett. **39**, 399 (1978).

[57] P. K. Mukherjee, Advances of isotropic to smectic phase transitions, J. Mol. Liq. **340**, 117227 (2021).

[58] S. Singh, Phase transitions in liquid crystals, Phys. Rep. **324**, 107 (2000).

[59] S. Kumar and S. K. Pal, *Liquid Crystal Dimers* (Cambridge University Press, Cambridge, UK, 2017).

[60] A. Brodin, A. Nych, U. Ognysta, B. Lev, V. Nazarenko, M. Škarabot, and I. Muševič, Melting of 2D liquid crystal colloidal structure, Condens. Matter Phys. **13**, 33601 (2010).

[61] T. C. Hales, A proof of the Kepler conjecture, Ann. Math. **162**, 1065 (2005).

[62] C. Vega, E. Paras, and P. Monson, Solid-fluid equilibria for hard dumbbells via Monte Carlo simulation, J. Chem. Phys. **96**, 9060 (1992).

[63] L. Onsager, The effects of shape on the interaction of colloidal particles, Ann. N.Y. Acad. Sci. **51**, 627 (1949).

[64] J. D. Parsons, Nematic ordering in a system of rods, Phys. Rev. A **19**, 1225 (1979).

[65] S.-D. Lee, A numerical investigation of nematic ordering based on a simple hard-rod model, J. Chem. Phys. **87**, 4972 (1987).

[66] L. Longa, P. Grzybowski, S. Romano, and E. Virga, Minimal coupling model of the biaxial nematic phase, Phys. Rev. E **71**, 051714 (2005).

[67] P. Karbowniczek, M. Cieśla, L. Longa, and A. Chrzanowska, Structure formation in monolayers composed of hard bent-core molecules, Liq. Cryst. **44**, 254 (2017).

[68] https://github.com/PKua007/rampack

[69] J. Goodby, R. Mandle, E. Davis, T. Zhong, and S. Cowling, What makes a liquid crystal? The effect of free volume on soft matter, Liq. Cryst. **42**, 593 (2015).